



NTNU – Trondheim
Norwegian University of
Science and Technology

Investigation of $\text{Co}_2\text{AlO}_4/\text{CeO}_2$ Catalyst for N_2O Abatement using Electron Microscopy Techniques

Ørjan Uteng Berntsen

Master of Science in Physics and Mathematics

Submission date: June 2014

Supervisor: John Walmsley, IFY

Co-supervisor: David Waller, YARA

Norwegian University of Science and Technology
Department of Physics

Preface

This thesis is a result of my diploma work at the Department of Physics, Norwegian University of Science and Technology (NTNU), Trondheim.

Through this project I have been given the opportunity to work with some of the best technological instruments in modern science, and to study materials down to their most fundamental properties. I have learnt to operate three different electron microscopes and used several different microscopy techniques. The work has given me much insight into empirical science and experimental work, and has been experience that I believe will be very useful for me beyond this thesis.

I wish to thank my supervisor John Walmsley for his kind support and valuable guidance throughout the project period. I would also like to thank Randi Holmestad for her help and support, Ruben Bjørge for TEM training, Bjørn Soleim for equipment training and generally assisting when in need, and the other helpful and accommodating people in the TEM group for being there and answering my questions. Thanks to Ken Roger Ervik at NTNU NanoLab for training on the SEM instrument. Also thanks to David Waller at Yara International ASA for valuable insight into catalysis research and engineering.

This thesis is written for my peers. A basic understanding of math and solid state physics is expected of the reader.

Trondheim, June 16, 2014

Ørjan Uteng Berntsen

Abstract

A N_2O abatement catalyst of a Co_2AlO_4 active phase and CeO_2 support phase has been investigated using transmission electron microscopy (TEM), scanning transmission electron microscopy (STEM) and scanning electron microscopy (SEM). The goal of the investigation was to link properties of the support material to the activity of the final catalyst. Six samples of the catalyst were investigated. Catalysts of two grades of support, a high surface and a low surface, were provided in three different variants each: support material only, complete fresh catalyst and used catalyst.

The high surface support material was found to be comprised of significantly smaller individual particles than the low surface support, as expected. This difference in support particles had evened out considerably to their respective complete unused catalysts, although the high surface catalyst still had somewhat smaller particle sizes. In the used catalysts the high surface samples had grown slightly while the low surface sample looked mostly unchanged. The Co_2AlO_4 phase was found to be comprised of particles that were typically in the size range 30-200 nm. Quantitative particle-size statistics were not obtained to confirm this because of low particle counts and low STEM Z-contrast. TEM images showed that Co_2AlO_4 particles had characteristic rough surfaces compared to the CeO_2 particles. Some Co_2AlO_4 particles also had fine nanoparticles on their surfaces. STEM/EDS analysis was employed to demonstrate the distribution of Co_2AlO_4 particles on the support in the high surface catalysts, and also indicated that many Co_2AlO_4 particles had become embedded partially or completely into the bulk of support particles, instead of residing on the surface.

It is suggested here that sintering of the support particles during calcination plays an important role for the activity and longevity of the catalyst. The active phase is also thought to undergo sintering during calcination. The surface roughness and nanoparticles observed on the Co_2AlO_4 particles could influence the effective surface area and thereby activity. The nanoparticles are believed to be of either the Co_2AlO_4 or the Co_3O_4 structure, but could not be conclusively determined. Their phase is believed to play an important role for the activity of the catalyst. The high degree of sintering of the high surface area support oxide during calcination could result in the observed embedding in the corresponding catalyst material. Embedding is believed to result in decreased initial activity but increased longevity of the catalyst.

Sammendrag

En katalysator for reduksjon av N_2O bestående av en aktiv komponent Co_2AlO_4 og en katalysatorbærer av CeO_2 har blitt undersøkt med transmisjonselektronmikroskopi (TEM), scanning transmisjonselektronmikroskopi (STEM) og scanning elektronmikroskopi (SEM). Undersøkelsen hadde som målsetning å finne hvilke egenskaper ved bærer materialet som påvirker katalysatorens aktivitet. Seks prøver ble undersøkt. Katalysatorer fra to ulike oksider, en med høy overflate og en med lav overflate, ble undersøkt i tre ulike prøver hver: kun bærer materialet, ubrukt ferdig katalysator, og brukt katalysator.

Høyoverflate-bæreren bestod som forventet av mye mindre partikler enn lavoverflate-bæreren. Denne ulikheten i partikkelstørrelser i bærer materialene hadde i stor grad blitt utjevnet i deres respektive ferdige katalysatorer, men katalysatoren basert på høyoverflate-bæreren bestod imidlertid fortsatt av noe mindre partikler. Av de brukte katalysatorene hadde høyoverflate-katalysatoren økt noe i partikkelstørrelse mens lavoverflate-katalysatoren fremstod omtrent uforandret. Co_2AlO_4 -komponenten bestod av partikler i størrelsesordenen 30-200 nm. Kvantitativ partikkelstørrelsestatistikk ble ikke innhentet pga. for få partikler og for lav Z-kontrast i STEM. TEM bilder viste en karakteristisk ru overflate på Co_2AlO_4 -partiklene i forhold til CeO_2 -partiklene. Noen Co_2AlO_4 -partikler hadde også nanopartikler festet til overflaten. STEM/EDS ble utnyttet for å undersøke spredningen av Co_2AlO_4 -partikler på bærer materialet i høyoverflate-katalysatoren, og resultatene indikerte også at mange Co_2AlO_4 -partikler muligens befinner seg delvis eller fullstendig i bærerpartiklens indre, istedet for å ligge på overflaten.

Det er foreslått at sintring av bærerpartiklene under kalsinering spiller en viktig rolle for katalysatorens aktivitet og levetid. Den aktive komponenten kan muligens også gjennomgå sintring under kalsinering. Den røe overflaten og nanopartiklene som ble observert på Co_2AlO_4 -partiklene kan ha innvirkning på den effektive overflaten og dermed på aktiviteten. Nanopartiklene er trodd å være av Co_2AlO_4 eller Co_3O_4 oksider, men dette kunne ikke fastslås med sikkerhet. Deres struktur kan være viktig for katalysatoraktiviteten. Høy grad av sintring i høyoverflate-bæreren under kalsinering kan resultere i den observerte omslutningen av de aktive partiklene i katalysatorprøvene. Omslutning kan gi forminsket initiell aktivitet men økt levelengde for katalysatoren.

List of Abbreviations

fcc: Face-Centered Cubic

bcc: Base-Centered Cubic

sc: Simple Cubic

NO_x: Nitrogen oxides

SCR: Selective Catalytic Reduction

VLM: Visible Light Microscope

TEM: Transmission Electron Microscope

HRTEM: High Resolution Transmission Electron Microscopy

SAED: Selected Area Electron Diffraction

DP: Diffraction Pattern

STEM: Scanning Transmission Electron Microscopy

BF: Bright-Field

DF: Dark-Field

ADF: Annular Dark-Field

HAADF: High Angle Annular Dark-Field

SEM: Scanning Electron Microscope

SE: Secondary Electrons

BE: Backscattered Electrons

EDS: Electron Dispersive (X-Ray) Spectroscopy

FEG: Field Emission Gun

CCD: Charge-Coupled Device

XRD: X-ray Diffraction

FFT: Fast Fourier Transform

XPS: X-ray Photoelectron Spectroscopy

AFM: Atomic Force Microscopy

Contents

1	Introduction	1
1.1	Background	1
1.2	Problem and Motivation	2
1.3	Thesis Structure	4
2	Theory	5
2.1	Catalysis	5
2.2	Crystallography	6
2.3	Diffraction in Crystals	8
2.4	Experimental Techniques	10
2.4.1	Transmission Electron Microscopy	10
2.4.2	Scanning Transmission Electron Microscopy	15
2.4.3	Scanning Electron Microscopy	19
2.4.4	Energy Dispersive X-ray Spectroscopy	20
2.5	The $\text{Co}_2\text{AlO}_4/\text{CeO}_2$ Catalyst	21
2.5.1	Crystal Structure of Ceria and Co_2AlO_4	22
2.5.2	Synthesis and Implementation	24
3	Method	27
3.1	Instrumentation	27
3.2	Samples and Sample Preparation	27
4	Results	29
4.1	SEM	30
4.2	TEM	34
4.3	STEM	41
5	Discussion	45
5.1	Particle Size and Morphology of the Support Phase	45
5.2	Particle Size and Morphology of the Co_2AlO_4 Phase	46
5.3	Embedded Particles of the Co_2AlO_4 Phase	48
6	Conclusion	53

Contents

7 Further Work	55
A Summary of XRD/BET Results by Åbø	59
B The Fourier Transform	60
C Edge and Screw Dislocations	61

Chapter 1

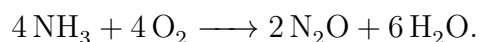
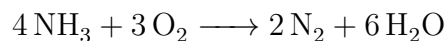
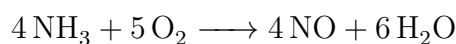
Introduction

1.1 Background

Nitric acid, HNO_3 , is an important constituent in the production of nitrogen fertilizers. Agriculture has in the modern age become increasingly dependent on such synthetic fertilizer in order to provide food to a rapidly growing world population. The effectiveness of inorganic synthetic fertilizers compared to that of the traditional organic fertilizers have made them a vital part of modern agriculture, often increasing crop yields significantly [1].

The popularity and high demand for synthetic fertilizers supports a large, worldwide, industry for the production of nitric acid, which is used to provide the nutritional nitrogen. However, byproducts of such a production are potentially harmful pollutants if released into the atmosphere, and a great emphasis therefore has to be put on abatement of these.

Many chemical reactions are involved to make up the total process of nitric acid production, but the reactions involved in the conversion of ammonia to nitric oxide (NO), in particular, are of great importance in an environmental perspective. This is due to the presence of nitrous oxide (N_2O):

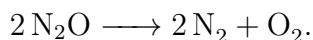


The reactions above show the possible pathways in the oxidation of NH_3 [2]. Of the three, the first reaction is the desired one, producing NO which is utilized further in the next step of the acid production. The second and third are unwanted, primarily

because they spend the reactant NH_3 , along with a great deal of energy, that should preferably have produced NO exclusively.

Unlike N_2 , which is a completely harmless byproduct and an inert gas which is in surplus in the atmosphere, N_2O is a particularly harmful gas. N_2O , or laughing gas, as it's commonly called, is both a greenhouse gas and an ozone depletion gas. Like carbon dioxide, methane and other greenhouse gases, the presence of nitrous oxide in the atmosphere increases global warming by absorption and emission of infrared radiation, effectively trapping solar energy in the atmosphere. While being one of the climate gases contributing the most to global warming today, N_2O is also the most important ozone-depleting emission of the 21st century [3] [4].

Nitrous oxide is decomposed in the reaction



N_2O gas is quite stable in room temperature and it has an estimated lifetime of 150 years in the atmosphere. Even at temperatures above 900°C the conversion is barely noticeable [5], which is about the temperatures typically involved in the oxidation process of NH_3 . A catalyst is therefore needed to increase the reaction rate of the decomposition in order to reduce the N_2O emissions.

1.2 Problem and Motivation

The 58-Y1 catalyst system, used for decomposing N_2O in gases containing NO , has been patented by Yara International ASA [6]. The catalyst is used in the ammonia oxidation process in connection with the production of nitric acid. It has an active component of a cobalt/aluminium oxide (Co_2AlO_4) which is supported on ceria (cerium dioxide, CeO_2). The catalyst was designed to be versatile, active and stable for a prolonged length of time, as well as thermally stable to withstand the operational conditions of the reactor.

Investigations by Yara into the catalyst system revealed that its performance varied widely with the source of the ceria used for support [2]. The results are plotted in Figure 1.1. The performance was found to be highly dependent on the support grade, i.e. if the oxide came from different suppliers or from different grades from a single supplier. In the investigation, different grades of the ceria support material were categorized based on their measured differences in surface-to-mass ratios, and were then used to make complete catalysts to investigate any impact on performance. It was expected that the performance of the final catalyst would improve for finer grades, as one of the main purposes for a support material is to provide a high surface area to the active phase. As seen in Figure 1.1, the oxide with the highest surface area was indeed found to be most effective, and this is the grade used in the commercially realised catalyst today. However, the performance did not scale

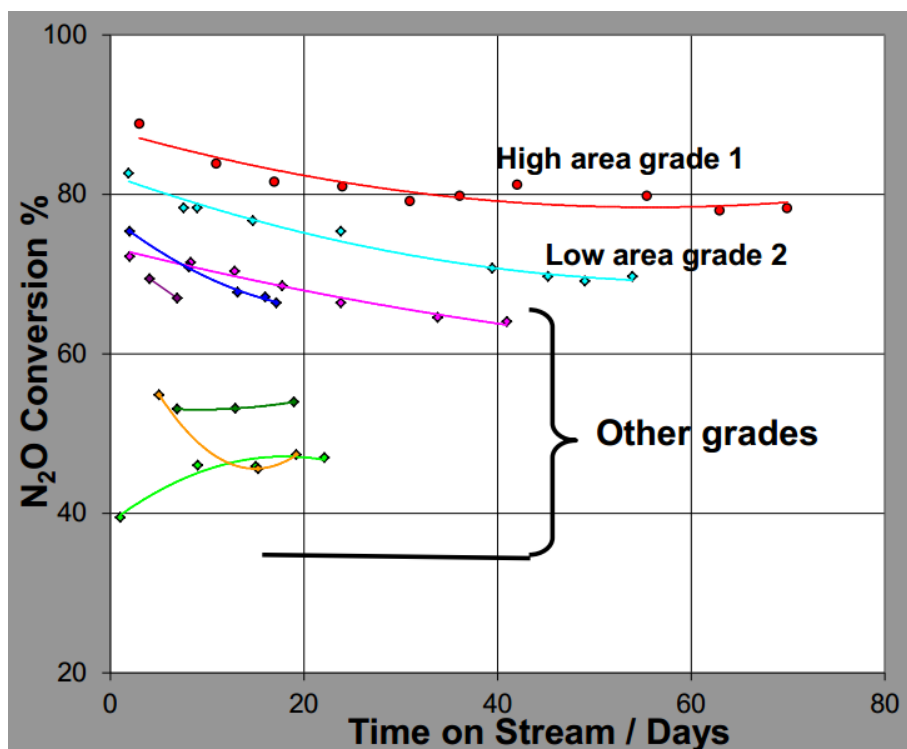


Figure 1.1: Results from the investigations by Yara showing the activity of catalysts made from different grades of support oxides as function of time on stream in a pilot reactor. The activity is measured in terms of N₂O conversion in stream. Graph from [2].

as expected with the surface area of ceria, as some cruder powders were found to outperform some of the finer ones, both in terms of immediate activity in conversion of N₂O, and in lasting stability in the reactor environment.

The results imply that some other properties than the surface area of the oxide influence the final effectiveness of the catalyst. Since finer grades of ceria are more difficult to produce and more expensive, it would be beneficial to employ a coarser oxide powder if some other property of the material was found to be the bottleneck for performance. In a broader perspective, understanding which properties of the support that influence the complete catalyst can help engineer a more effective catalysis in N₂O abatement in the production of nitric acid, and thereby reduce the greenhouse gas emissions from this industry.

In this project, the support and complete catalyst was investigated using transmission electron microscopy (TEM) and complementary methods. The goal was to identify which properties of the support that influence the effectiveness of the final catalyst, if not the surface area. Firstly, two grades of catalyst support material that were known to give differently performing final catalysts was examined ('high area grade 1' and 'low area grade 2' of Figure 1.1). Secondly, the complete catalysts,

made with the respective supports, were investigated. Samples of both fresh and used catalysts were looked at.

This thesis work has been in parallel with the thesis of Karl Magnus Åbø at the Department of Chemical Engineering, NTNU, who studied the same catalyst materials from a chemical perspective.

1.3 Thesis Structure

The thesis is divided into 7 main chapters, including this introduction. In the Theory chapter, the theory of relevance to the topics discussed in this report will be presented. The Method chapter will present the instrumentation used for experimental work, and sample preparation procedures. The obtained results will then be presented in the subsequent chapter. In the Discussion chapter, the results will be discussed and interpreted with respect to the problem. Finally, the Conclusion chapter will summarise the thesis and the most important findings, before suggestions for further work are presented.

Chapter 2

Theory

This chapter covers the theory that is relevant to this project. A basic introduction to catalysis is given, before the most important aspects of crystallography and diffraction theory are presented. The experimental techniques transmission electron microscopy (TEM), scanning transmission electron microscopy (STEM), scanning electron microscopy (SEM) and energy dispersive X-ray spectroscopy (EDS) are then introduced. Finally, the catalyst materials are presented and discussed in terms of crystal structures and known applications.

2.1 Catalysis

This section is based on the description given in Zumdahl [7]. A catalyst is a substance that increases the rate of a chemical reaction. By decreasing the activation energy, at a given temperature, the reaction rate increases. The catalyst material itself is not spent or changed in the chemical reaction it catalyses, and neither does it change the reaction formula. The actual mechanism with which it interacts between reactant and product is not necessarily known, but the effect is always to decrease the activation energy of the reaction. The energy difference between the reactants and products is not affected, but the free energy needed to pass the transition state of the reaction is lowered. This is illustrated on the energy pathway diagram of Figure 2.1.

Catalysts are classified as either homogeneous or heterogeneous, depending on their physical state compared to that of the substance they catalyse. A heterogeneous catalyst, which will be discussed in this project, is in a different phase to that of its reactants/products, for instance as a solid catalysing a gas. In that case the catalysis typically involves the gas-phase reactants adsorbing on a surface containing the catalyst, then migrating and reacting along the surface, and finally desorbing from it as the reaction product. The effectiveness of a catalyst is generally dependent

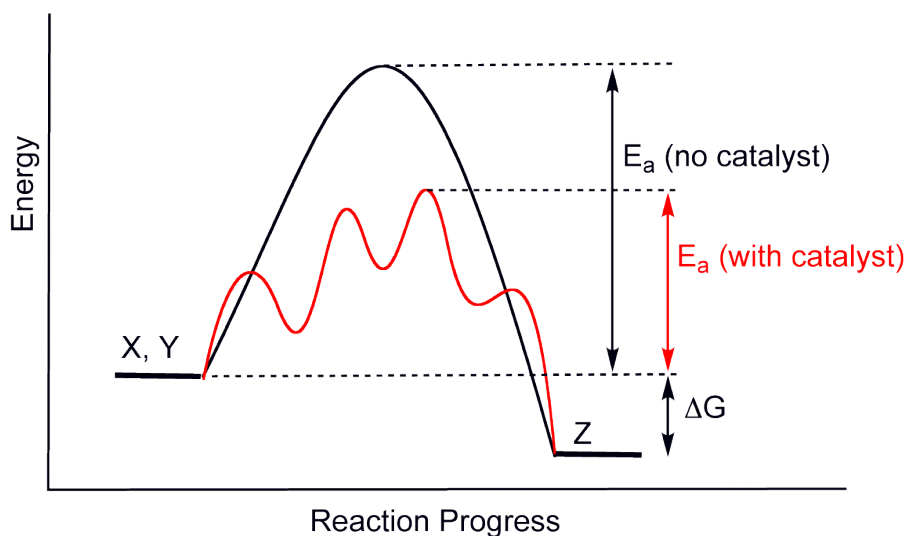


Figure 2.1: Energy pathway diagram for a reaction with and without catalysis. The activation energy E_a is decreased for the catalysed reaction process. Image from [8]

on the effective surface area of the active catalyst material to the reactants. Three main requirements are always important when developing a catalyst: the activity in regards to the intended reaction, the selectivity or ability to 'steer' a reaction towards the desired product, and its stability and longevity in the reaction conditions.

Catalysts have been effectively used for industrial purposes throughout the 20th century, and are today considered essential to almost all industrial chemical processes. It is only in the last few decades, however, that catalysts' importance for environmental purposes has been recognized. Examples include the catalytic converter used in automotive exhaust systems, and catalysts introduced to control the NOx gas byproduct produced in Nitric Acid plants such as the Selective Catalytic Reduction (SCR) system [9].

2.2 Crystallography

Materials can be categorized by their degree of structural order on the atomic level. Amorphous materials have no apparent order, other than some preferred radial distribution of atoms. Other materials have crystal ordering, where the same 'building block' of atoms is repeated in a predictable manner. This is found in many solids like metals and oxides. A crystalline material is one that exhibits a periodic pattern in its atomic positions that can be described by a lattice. A crystal lattice is mathematically described by the vector

$$\mathbf{r}_m = m_1\mathbf{a} + m_2\mathbf{b} + m_3\mathbf{c}, \quad (2.1)$$

where \mathbf{a} , \mathbf{b} and \mathbf{c} are the lattice vectors and m_1 , m_2 and m_3 are integers. Equation 2.1 describes a Bravais lattice; an infinite lattice such that for any permutation of \mathbf{r}_m , the lattice will look the same. Although any real crystal must be finite, it is often useful to consider a Bravais lattice when discussing its structure.

The periodically repeating atomic cell in a crystal structure is called the unit cell, which contains the basis, and when translated and repeated will fill up all space. The unit cell with the minimum volume is called the primitive cell and contains only one lattice point. However, in many cases it is more convenient to define a so-called conventional cell that can contain more lattice points.

At each lattice point there is located a basis, which is the repeating fragment in a lattice and may contain one or more atoms. The basis has a symmetry that defines its point group, i.e. a set of symmetry operations that can be performed on it. The operations are such that they leave one point fixed while moving other features to new position, returning the exact same geometry. The operations include rotations, inversions and reflections. The point group symmetry and the translational symmetry of the lattice together make up the space group of the crystal structure. There are a total of 32 crystallographic point groups and 230 crystallographic space groups that are possible.

Crystal structures are for convenience divided into general classes based on the point group called crystal systems, that describe the shape and restrictions on the unit cell. All space groups are contained within these systems. The different systems and their restrictions are listed in table 2.1.

Table 2.1: The 7 crystal systems with their respective conventional cell axes and angles restrictions.

Crystal system	Axis restrictions	Angle restrictions
Triclinic	$a \neq b \neq c$	$\alpha \neq \beta \neq \gamma$
Monoclinic	$a \neq b \neq c$	$\alpha = \gamma = 90^\circ \neq \beta$
Orthorombic	$a \neq b \neq c$	$\alpha = \beta = \gamma = 90^\circ$
Tetragonal	$a = b \neq c$	$\alpha = \beta = \gamma = 90^\circ$
Cubic	$a = b = c$	$\alpha = \beta = \gamma = 90^\circ$
Trigonal	$a = b = c$	$\alpha = \beta = \gamma < 120^\circ, \neq 90^\circ$
Hexagonal	$a = b \neq c$	$\alpha = \beta = 90^\circ, \gamma = 120^\circ$

A useful concept in crystallography is the reciprocal lattice, which is a corresponding lattice representation in *reciprocal space*. The reciprocal lattice \mathbf{r}^* is defined by the relation

$$e^{i\mathbf{r} \cdot \mathbf{r}^*} = 1. \quad (2.2)$$

It follows that, for a real space lattice \mathbf{r} , the reciprocal lattice must take the

form

$$\mathbf{r}^* = h\mathbf{a}^* + k\mathbf{b}^* + l\mathbf{c}^*, \quad (2.3)$$

where h , k and l are the integer Miller indices. The reciprocal lattice vectors are defined from the real space vectors as

$$\begin{aligned} \mathbf{a}^* &= \frac{2\pi}{V}(\mathbf{b} \times \mathbf{c}) \\ \mathbf{b}^* &= \frac{2\pi}{V}(\mathbf{c} \times \mathbf{a}) \\ \mathbf{c}^* &= \frac{2\pi}{V}(\mathbf{a} \times \mathbf{b}) \end{aligned} \quad (2.4)$$

where $V = \mathbf{a} \cdot (\mathbf{b} \times \mathbf{c})$ is the unit cell volume. An example is shown in Figure 2.2, where a face-centered cubic (fcc) unit cell is displayed, along with its corresponding reciprocal lattice structure, the base-centered cubic (bcc). fcc, bcc and simple cubic (sc) are the three lattice types of the cubic crystal system.

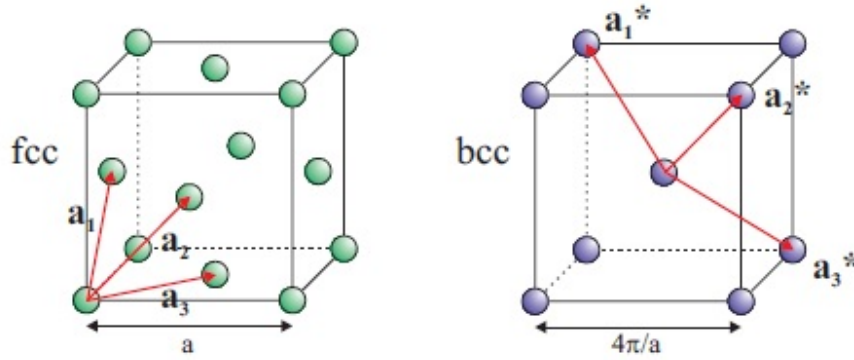


Figure 2.2: A fcc crystal unit cell and its reciprocal counterpart, the bcc unit cell. Both are conventional unit cells. Conversely, the bcc unit cell in real space has a corresponding fcc structure in reciprocal space. Notice that a slightly different notation of the lattice vectors have been used. Image from [10].

The Miller indices hkl in (2.3) defines a lattice point of the reciprocal lattice. To each lattice point there is a corresponding plane (or a set of planes) in the real space crystal. A plane in real space is denoted (hkl) , and it will cut the unit cell axes a , b and c at relative positions $1/h$, $1/k$ and $1/l$, respectively. In this notation it is conventional to write negative values with a bar, e.g. $-1 = \bar{1}$. Examples of planes from different hkl -values are shown in Figure 2.3.

2.3 Diffraction in Crystals

Diffraction of waves from a crystal can occur under certain conditions as described by the Laue criteria,

$$\mathbf{Q} = \mathbf{g}_{hkl}. \quad (2.5)$$

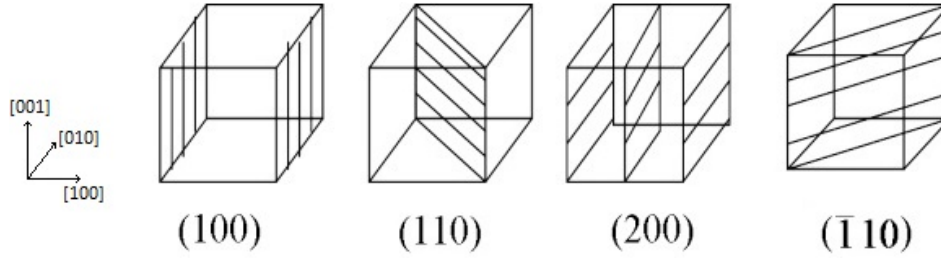


Figure 2.3: Examples of planes (hkl) in a crystal structure. Image from [11]

$\mathbf{Q} = \mathbf{k}_f - \mathbf{k}_i$ is the wavevector transfer from the incoming and final wavevectors, \mathbf{k}_i and \mathbf{k}_f respectively, and $\mathbf{g}_{hkl} = (h\mathbf{a}^* + k\mathbf{b}^* + l\mathbf{c}^*)$ is a vector in reciprocal space.

Diffraction can be pictured by Bragg's Law, which illustrates how two incoming beams of equal phase and wavelength are diffracted from parallel planes separated by a distance d_{hkl} . A sketch of the situation is seen in Figure 2.4. Bragg's law can

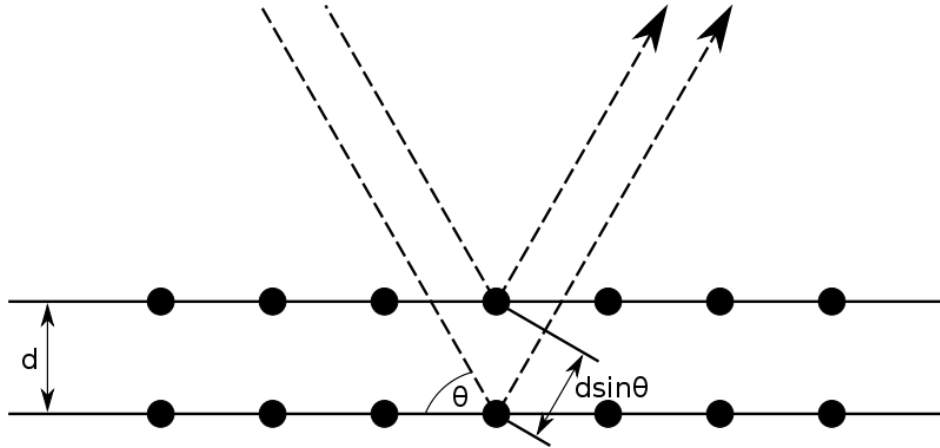


Figure 2.4: Two beams of equal wavelength and phase are scattered from two planes. The incoming beams are scattered by an angle θ , and the planes are separated by a distance $d = d_{hkl}$. Image from [12]

be derived from the figure as

$$n\lambda = 2d_{hkl} \sin \theta_B, \quad (2.6)$$

where λ is the wavelength and θ_B is the Bragg angle of diffraction for a n 'th order scattering. For high energy electrons, the relativistic de Broglie wavelength of an electron is given by [13]

$$\lambda = \frac{h}{\sqrt{2m_0eV(1 + \frac{eV}{2m_0c^2})}}, \quad (2.7)$$

where h is Planck's constant, m_0 the electron rest mass, e the electron charge, V the acceleration voltage and c the speed of light.

The interplanar spacing d_{hkl} in Eq. 2.6 is defined as the minimum distance from the unit cell origin to the plane, and is generally given by

$$d_{hkl} = \frac{2\pi}{g_{hkl}}. \quad (2.8)$$

For crystalline materials in a cubic structure of lattice parameter a , the interplanar spacing simplifies to

$$d_{hkl} = \frac{a}{\sqrt{h^2 + k^2 + l^2}}. \quad (2.9)$$

The amplitude of each reflection in reciprocal space is found from the structure factor,

$$F_{hkl} = \sum_j f_j e^{2\pi i(hx_j + ky_j + lz_j)}, \quad (2.10)$$

where f_j is the atomic form factor and x_j, y_j and z_j are the relative coordinates in the unit cell, and the sum runs over all atoms in the basis. Eq. (2.10) is only valid for kinematic scattering, i.e. that only a single scattering event has occurred. For electron radiation, the form factor generally increases with the atomic number Z of the atom, as they interact strongly with both the electron cloud and the charged nucleus. The intensity in reciprocal space is proportional to the modulus squared of the structure factor, $I \propto |F_{hkl}|^2$.

2.4 Experimental Techniques

This section introduces the different electron microscopy techniques that were utilized in this study. Transmission electron microscopy (TEM) was the main technique used to study the samples and is presented in a little more detail. Scanning transmission electron microscopy (STEM) was used for analytical imaging and elemental mapping of the catalyst. Scanning electron microscopy (SEM) was performed for surface characterisation of particles. Energy dispersive X-ray spectroscopy (EDS) was used in tandem with both TEM and STEM for compositional analysis.

2.4.1 Transmission Electron Microscopy

The Transmission Electron Microscope (TEM) is a powerful imaging and analysis tool in materials science. As the name implies, TEMs utilise electrons to 'illuminate' the sample, unlike the electromagnetic radiation of the traditional Visible Light Microscope (VLM). For VLM, the smallest distance that can be resolved is given approximately by the Rayleigh equation [13],

$$\delta = \frac{0.61\lambda}{\mu \sin \beta}, \quad (2.11)$$

where λ is the photon wavelength, μ is the refractive index of the viewing medium and β is the lens' semi-angle of collection. From this, it can be found that the VLM can only dissolve distances down to a few hundred nanometers. High-energy electrons used in TEM have a much smaller wavelength (the de Broglie wavelength) than visible light, and one can achieve a much higher resolution. This is one of the main motivations for using electrons instead of light.

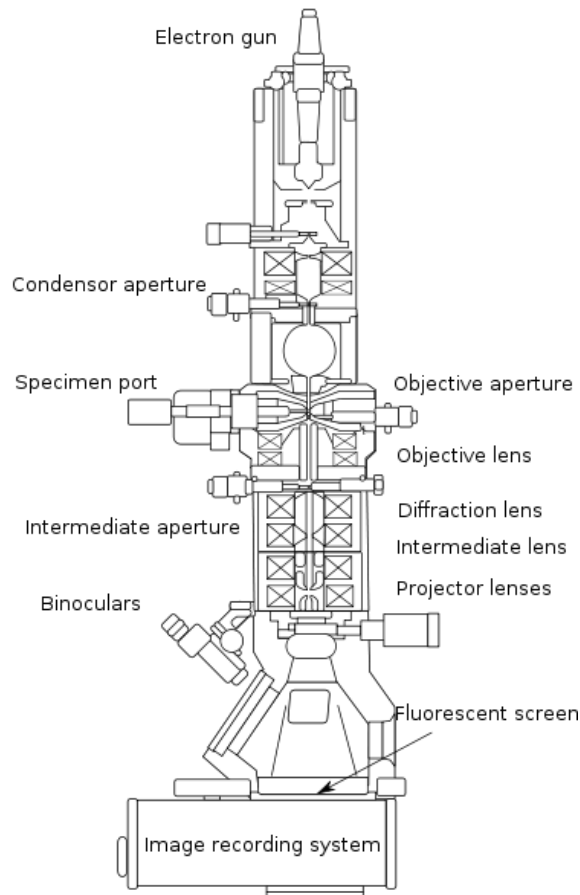


Figure 2.5: TEM hardware and setup. Image from [14].

The TEM instrument is a complex piece of equipment that consists of many lenses and other components, each serving a different specific purpose. A typical column setup of a TEM is shown in Figure 2.5. The illumination source is usually called the electron gun or the filament and is placed on the top of the column. Electrons are emitted as a beam from the filament and accelerated downwards by the acceleration voltage. The condenser system sits below, and consists of the condenser lens and aperture (or diaphragm) that concentrate and reduce spherical aberrations of the electron beam. The beam then illuminates and interacts with the sample that is inserted into the column with a sample holder. Then follows the objective stage with the objective lens and aperture. The objective lens is the most important lens in

the image formation, and follows immediately after the specimen stage. Below the objective stage there is a selected area aperture and a range of intermediate lenses and projection lenses. Finally the beam reaches the imaging stage, where it can be projected onto fluorescent viewing screen or a CCD camera.

Interactions: Scattering and Diffraction

Going through the specimen material, the negatively charged electrons of the radiated beam interact with electron clouds and nucleus of the atoms in the specimen, and scatter. These interactions are crucial to the TEM operation; it would be impossible to form images if the electrons didn't interact with the specimen to deviate their course.

Interactions must be explained by the particle/wave duality exhibited by electrons, and they could be regarded as one or the other depending on the effect in question. In the particle representation, electrons are said to undergo scattering events when interacting with the specimen. In TEM, electrons are typically scattered both elastically and inelastically, so that each particle could either retain its energy or lose some of it in the event. If the latter occurs, the energy is transferred to the sample and causes phonons, plasmons or ionization.

From a wave point of view, the electron beam is diffracted when interacting with matter. Diffraction can either be coherent or incoherent, which is typically the result of elastic and inelastic scattering events in the particle analogy, respectively. As a result of these interactions, many different signals are emitted and can be acquired from the sample, as can be seen in Figure 2.6.

The probability of an electron scattering is closely related to the cross section it "sees" going through the specimen,

$$\sigma_T = \sigma_{elastic} + \sigma_{inelastic}. \quad (2.12)$$

The cross sections typically depend on the atomic number of atoms present in the sample, angle of incidence of the electron (i.e. its path in respect to the specimen orientation), and the energy of the electron.

If the electron is scattered only once going through the material, it is said to have undergone kinematic scattering. If more scattering events occur it is called dynamical scattering. Kinematic scattering is generally preferred in TEM as it is less complicated and more easily interpretable. Nonetheless, due to the strong interaction between electrons and matter, dynamical scattering is very common and its effects often noticeable. As dynamical scattering is more likely for thicker samples it is advantageous to have as thin samples as possible.

The fact that electrons transmit through the specimen while scattering and diffracting with the specimen material gives TEM other capabilities than the absorption

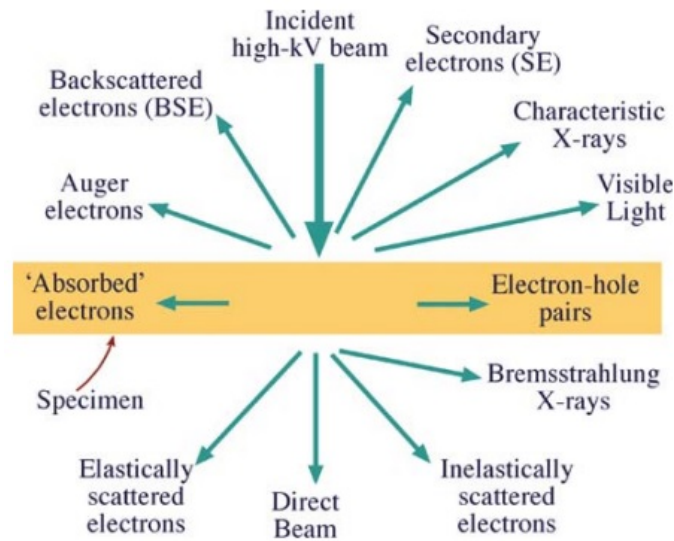


Figure 2.6: Sketch of different signals generated when a sample is radiated by an electron beam. Image taken from Williams and Carter [13].

based VLM, especially when it comes to crystalline materials. Probing the inside of the specimen and interacting with the atoms and their systematic configuration makes it possible to analyse characteristics such as the crystal structure of a crystalline material. This also means that the 2D projection image taken by transmitted electrons of a 3D physical object must be carefully interpreted, as the features seen in an image can be attributed to many different effects when averaged through the sample.

There are different mechanisms that give contrast in TEM images. Diffraction contrast is the specific contrast mechanism caused by elastic and coherent Bragg scattering. This is the contrast that occurs from difference in crystal structure and orientations as they scatter differently. Phase contrast is also common due to the prominence of elastic and coherent scattering of electrons. Here, the phase relationship between scattering events cause spatial fluctuation and inversion of contrast in the observed intensity. This is the origin of contrast features such as lattice fringes and thickness fringes that are observed in images. Another important contrast mechanism is the mass-thickness contrast, which is the result of incoherent elastic Rutherford scattering. Mass-thickness contrast stems from the fact that thicker parts of a sample, and denser materials of heavier atoms and higher Z , scatter more.

Modes of Operation

Selected area electron diffraction (SAED) is an important operation mode for TEM, complementing the direct space imaging and in many situations giving information

beyond what can be observed there. The diffraction pattern of the material can be imaged by configuring the lenses such that the back focal plane is in focus rather than the image plane. The selected area aperture is used to restrict the area of the specimen illuminated, so that one can observe the diffraction resulting from a very specific area, down to some tens of nanometers. A ray diagram for SAED is displayed on Figure 2.8b.

In the geometrical and optical conditions of TEM diffraction mode, the interplanar spacing of scattering planes can be found by

$$d_{hkl} = \lambda \frac{L}{R_{hkl}}, \quad (2.13)$$

where L is the *camera length* (optical distance from specimen to camera) and R_{hkl} is the measured distance from the direct beam to the reflection, assuming small angles ($R_{hkl} \ll L$). The geometry is depicted in Figure 2.7.

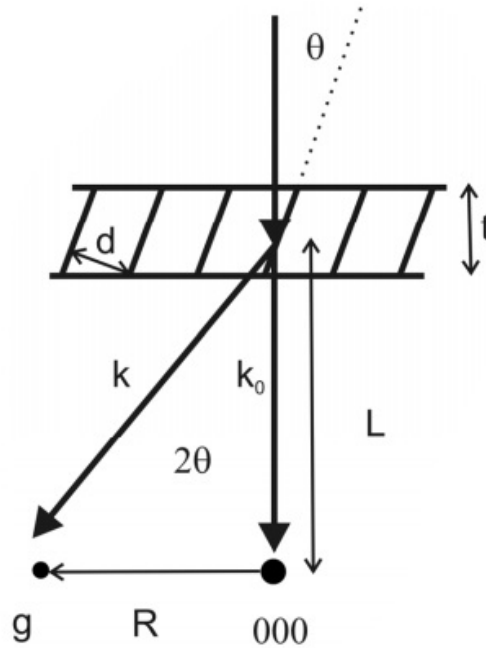


Figure 2.7: Sketch of scattering from planes of spacing d in a sample of thickness t to an angle 2θ onto a detector screen in a TEM. The sketch includes the camera length L and the reflection distance R from the direct beam 000 to a reflection g . In modern TEMs the camera length L is not an actual distance, but an optical distance induced by intermediate lenses.

The ability to change between direct imaging and diffraction mode on the fly for a specific area under inspection is one of the strengths of TEM. Controlling the diffracted parts of the electron beam can also be used to influence the direct space

image. The Objective Aperture can be used to exclude certain reflections of the diffracted beam, and the rays can then be brought back by subsequent lenses to display an image of different contrast. If a particular area of the sample is scattering to these excluded reflections, this area will appear dark when rays are brought back to the image. In bright field (BF) imaging, everything but the direct beam is excluded. This results in a loss in observed intensities to areas that scatter in the sample, increasing diffraction contrast and removing phase contrast. Figure 2.8(a) shows the ray diagram for BF imaging. Conversely, the aperture can be set to pass only a certain reflection, and areas scattering into that particular spot retains their intensities while all other areas fade. This is called dark field (DF) imaging. The names refer to the appearance of vacuum (which does not scatter electrons) as bright in BF and dark in DF.

Lattice Fringes and Moiré fringes

Phase contrast is the most important contrast for High Resolution TEM (HRTEM). Of particular relevance are the lattice fringes that appear in crystalline materials. The effect can be demonstrated by considering an interference between the direct beam at $\mathbf{0}$ and a Bragg reflection beam at \mathbf{g} . It can be shown that the observed intensity of the interfering beams is (with some approximations) [13]

$$I = A^2 + B^2 - 2AB \sin(g'x - \pi st), \quad (2.14)$$

where x is the position on an axis normal to \mathbf{g} , A and B are constant factors (with respect to x) and t the thickness of the sample. s is the magnitude of the deviation vector \mathbf{s} , and $g' = |\mathbf{k}_I + \mathbf{s}|$, \mathbf{k}_I being the incoming wavevector of the direct beam. This is then a sinusoidal variation in intensity along an axis parallel to \mathbf{g} with wavelength $2\pi/g'$. In the case of $s = 0$ we have that $g' \rightarrow g$, and so the wavelength of the intensity variation in I will be equal to that of the lattice since $g = 2\pi/d$ from (2.8). An image with crystals displaying lattice fringes is given in Figure 2.9.

In areas where many different crystals are visible, it is normal that two different crystals overlap such that their lattice fringes interfere. If the fringe periodicity of the crystals are almost equal, this can result in Moiré fringes. These are coarser fringes with larger spacings and a different rotation from the fringes from which they originate. Many of the coarser fringes seen in Figure 2.9 are Moiré fringes caused by underlying lattice fringes.

2.4.2 Scanning Transmission Electron Microscopy

Scanning transmission electron microscopy (STEM) is a valuable complementary method to traditional TEM imaging. Here, the sample is illuminated by a well converged electron beam, or 'probe'. The beam is run over the area of the sample

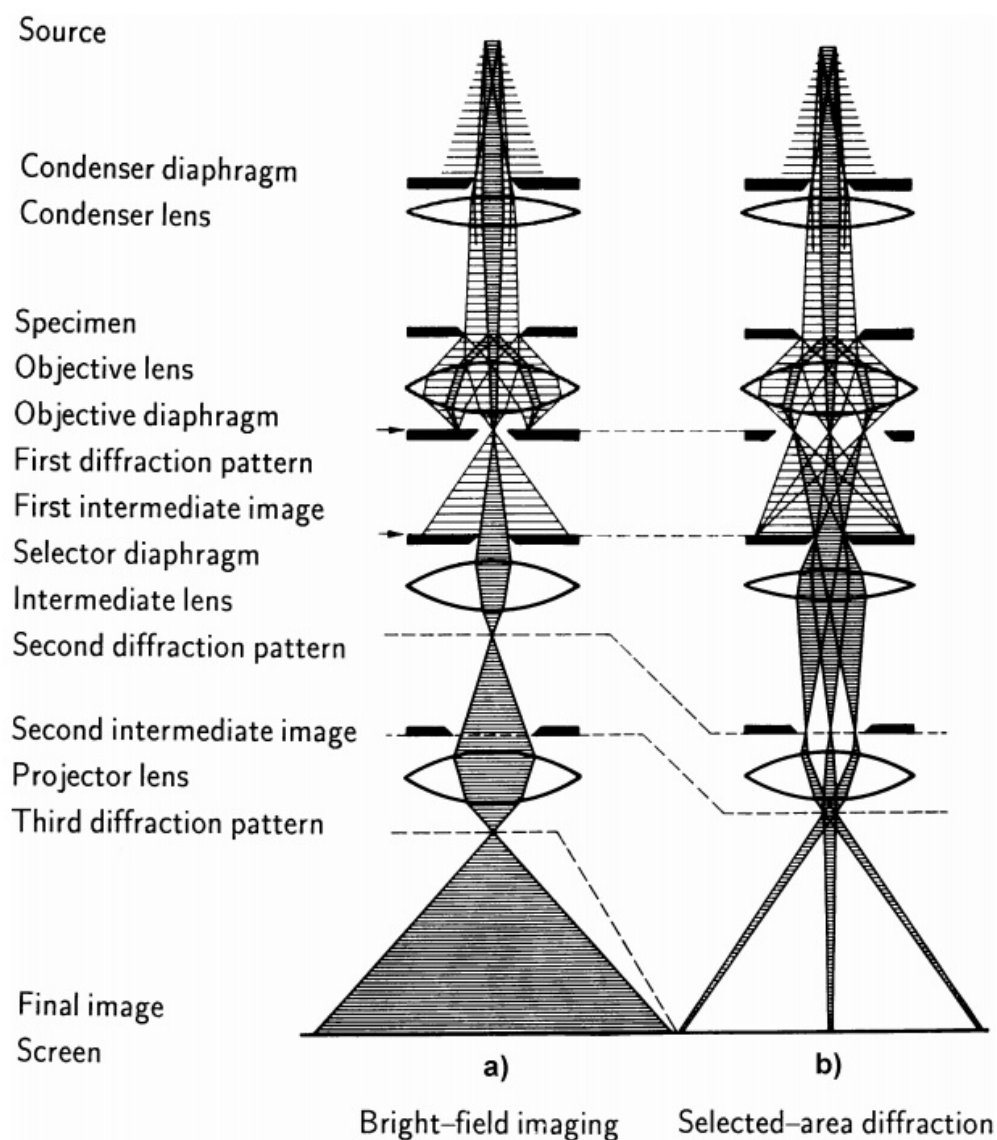


Figure 2.8: Ray diagrams for a TEM in (a) BF mode and (b) SAED mode. Apertures are here called diaphragms, which is referencing the physical stop rather than the hole. The selected area aperture is called selector diaphragm in this figure. Image from Reimer and Kohl [14].

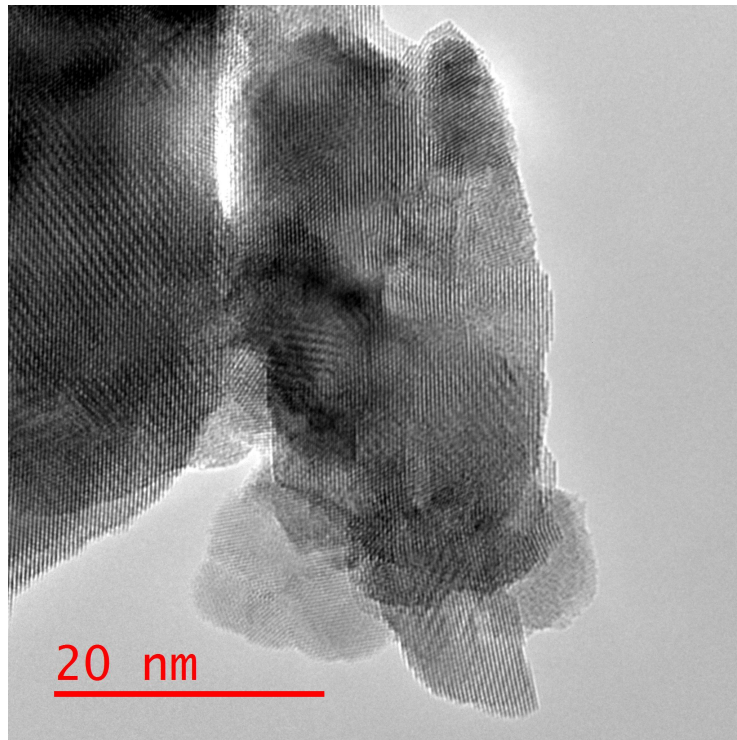


Figure 2.9: Example TEM image showing crystal grains that display lattice fringes and Moiré fringes. This image is taken from the low surface support oxide material (LS-s).

being investigated, quickly scanning it in raster fashion. Signals are collected with annular detectors as a function of position, and the detected intensities are then used to build an image. One of the strengths of STEM is its analytical power in that it provides elemental contrast, making it suitable for characterising different chemical phases in a material. The schematic arrangement of the instrument is depicted in Figure 2.10.

STEM uses annular detectors to detect the transmitted electron beam at different angles from the optical axis. A Bright Field (BF) detector detects the unscattered and very low angle scattered electrons. Imaging in STEM BF is closely related to conventional TEM (CTEM) by the principle of reciprocity, saying that propagation of electrons through the optical system is time reversible for elastic scattering. The optics of bright field conditions in STEM is the equivalent of CTEM, but with an electron source scanning across the original detector positions and the BF detector at the original source position. Thus, the contrast mechanisms in STEM BF is the same as in CTEM, with coherent imaging giving phase contrast from interference [15].

Annular Dark Field (ADF) detects electrons that are scattered to higher angles, ignoring all low angle signals. The most important difference between BF and ADF

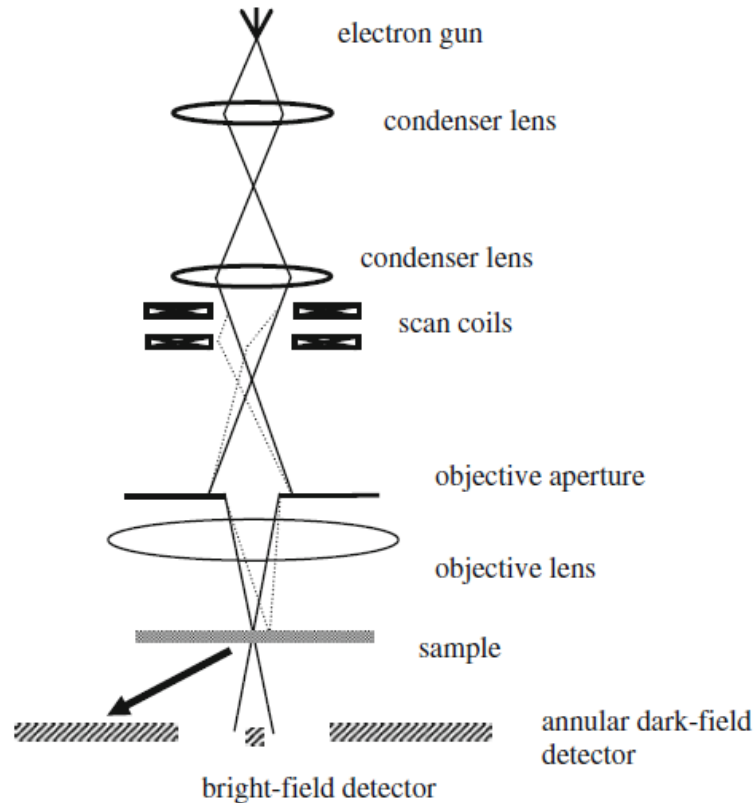


Figure 2.10: Schematic STEM instrument setup with the most important elements. Figure from [15].

in STEM is that the latter is an incoherent imaging mode. The incoherency is mainly a result of two contributing factors. Firstly, by using a large detector geometry, the effects of spatial coherency in the scattering is effectively averaged out. By reciprocity this is equivalent to a CTEM with a large source, which would also result in incoherent illumination. Secondly, when electrons are detected at higher angles they have predominantly undergone thermal diffuse scattering (TDS), which is uncorrelated between atoms, and further 'washes out' any phase dependency. Thus, the coherent effects of elastic scattering can be neglected and we have incoherent imaging [15]. Dynamical scattering is also incoherent, and the contrast reversals seen in HRTEM due to sample thickness (thickness fringes) are not present in STEM ADF [16].

Image contrast in ADF stems from the fact that heavier atoms with more positively charged cores will scatter electrons to higher angles (mass-thickness contrast). Therefore the contrast is highly dependent on the elements that scatter in the sample. This is commonly referred to as Z-contrast in STEM. Phase contrast can still occur in ADF to some extent, but if one increases the camera length to collect from higher angles with High Angle Annular Dark Field (HAADF), all coherency will be

removed and Z-contrast further increased.

The difference between coherent and incoherent imaging is nicely demonstrated by their mathematical descriptions. If a sample is illuminated by a coherent plane wave, coherent imaging can be defined by the intensity function

$$I_{coh}(\mathbf{R}) = |P(\mathbf{R}) * \psi(\mathbf{R})|^2, \quad (2.15)$$

where $P(\mathbf{R})$ is a point-spread function and $\psi(\mathbf{R})$ is the exit surface wavefunction, at position \mathbf{R} [17] [15]. The convolution with P is due to lens aberrations and results in a smearing of the two functions. Since this is a complex amplitude, spatially separated parts of the specimen can interfere as the convolution is integrated, resulting in the coherent imaging effects. Incoherent imaging is described as a convolution between the absolute squares (intensities) of P and ψ ,

$$I_{incoh}(\mathbf{R}) = |P(\mathbf{R})|^2 * |\psi(\mathbf{R})|^2. \quad (2.16)$$

Unlike (2.15), (2.16) does not include the phase properties (imaginary part) of the functions in the convolution, hence there is no coherency between different parts of the specimen.

2.4.3 Scanning Electron Microscopy

Scanning electron microscopy (SEM) is an electron microscopy technique well suited for surface characterization. It operates at a lower acceleration voltage compared to the TEM, so the electrons will typically not have enough energy to transmit through materials. Instead they interact at or near the material's surface by being absorbed. The material then emits signals from its surface that can be detected and used for imaging purposes [18].

SEM uses a converged electron beam to quickly scan the selected area of the sample. The SEM then detects the signals from each different scanning position of the probe and builds a complete image.

The signal detected is usually electrons that escape from the material being ionized by the electron beam. The standard signal used is from the secondary electrons (SE). These originate from shallow in the material and give great surface detail and topological information. Backscattered electrons (BE) are also an important signal source in SEM. BEs can provide elemental contrast, though normally at the expense of resolution since the electrons are more energetic and thus can escape from a larger area around the probe.

The schematic setup is similar to the STEM illustration in Figure 2.10, except for the SE and BE detectors which are located above the sample in SEM.

SEM images from SE are often more intuitively interpretable compared to TEM images. The position of the detector makes electrons escaping a surface facing it

more easily detected, and the result is a shadow effect that makes the object seem illuminated from one side. Observing a surface is what is experienced in daily life with reflected visible light, and SEM images are therefore comparable to traditional photography or even human vision from an intuitive point of view.

2.4.4 Energy Dispersive X-ray Spectroscopy

EDS is a powerful analytical technique that can be applied for chemical characterization in both TEM and STEM. It utilizes inelastic scattering events between the electron beam and sample to provide information about the elemental composition in the sample.

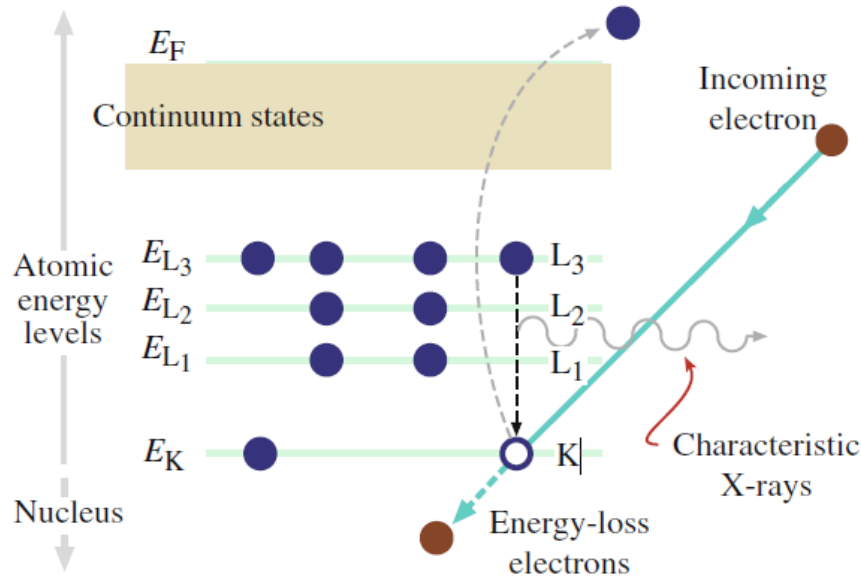


Figure 2.11: Ionisation and subsequent X-ray radiation due to inelastic scattering events. An electron in the K-shell is here ionised, causing an L-shell electron to de-excite. The energy difference is then radiated as characteristic X-ray photon, in this case a so-called K_α transition. Figure from Williams and Carter [13].

When an inner orbital electron of an atom interacts with a high energy electron from the beam, the energy transferred to the shell electron can lift it out of the nuclear potential. The atom is then left in a highly energetic ionized state. Since atoms prefer to exist in their lowest possible energy state, it will readily de-excite by transitioning an electron occupying a higher orbital to the now available low energy state. This is illustrated in Figure 2.11.

De-excitation will in general occur as a cascade of successive transition events, where the higher energy electron subsides into and reoccupies the now available lower

energy state, which leaves an available orbital that can be replaced again, and so on. The excess energy of the transition is released either as electromagnetic radiation or as an Auger electron. Since different atomic elements have orbitals of unique energy, energy differences between states are also unique to the element. Hence, when an atom de-excites as electromagnetic radiation, the radiated photon's energy is characteristic to that specific element. The energy $h\nu$ of the photon is equal to the difference in energy from orbital n' to n'' ,

$$E_{n'} - E_{n''} = h\nu. \quad (2.17)$$

Different energy transitions of an element also have different statistical probabilities of occurring (although subject to experimental conditions). The X-ray peaks' energies and relative intensities are characteristic to their specific element, making it possible to identify different elements. However, it can not provide information about the chemical structure because of the inherent low energy resolution of the X-rays, making energy shifts due to chemical bonds unresolvable.

In microscopes, the X-rays are collected by inserting the detector into the column vacuum. There it is exposed to the radiation for a specified duration. With modern software it's a simple task to identify the elements present from the acquired X-ray spectrum. In TEM, the total illuminated area of the sample will contribute to the EDS spectrum. By condensing the electron beam one can investigate the composition of smaller areas of the specimen with relative ease.

EDS is particularly useful when combined with STEM. With the probe scanning the sample area systematically and repeatedly, X-ray data can be collected from each position. Thus one can spatially resolve the elemental compositions and form a compositional map of the area. This is a very useful technique to characterize different phases in a sample.

2.5 The $\text{Co}_2\text{AlO}_4/\text{CeO}_2$ Catalyst

This section will introduce the two material phases that are present in the catalyst which was investigated.

The complete catalyst from Yara contains about 2 mole-percentage of the active material Co_2AlO_4 , the rest being ceria support. Cobalt has the atomic number $Z_{\text{Co}} = 27$, aluminium $Z_{\text{Al}} = 13$, and cerium $Z_{\text{Ce}} = 58$.

The active phase was developed from the baseline cobalt oxide spinel Co_3O_4 [2]. However, under high temperature and low oxygen conditions the phase was found to reduce to CoO . A substitution of Al into the structure was found to produce more stable phases, with the stoichiometric composition Co_2AlO_4 the most stable.

One of the most important applications of cobalt in catalysis is in the Fischer-Tropsch process for hydrogenation of carbon monoxide, which is used for GTL (gas to liquid) conversion, among other applications [19] [20]. Cobalt's catalytic capabilities with regards to nitrous oxide decomposition is well known [21].

Ceria has previously been used both as an active catalyst and as a catalyst support material for different reactions. As a catalyst, the ceria has important features like high ion mobility, the ability to switch between the Ce^{3+} and Ce^{4+} cations non-stoichiometrically while retaining its structure, as well as having a high oxidizing power [22]. It has also been used as an oxygen storage material in automotive catalysts because of this ability to readily change its redox state [23].

As a catalyst support, the role of ceria is to provide a surface area onto which catalytic particles can disperse and stabilize. For all heterogeneous catalyst it is desirable to expose as much surface of the active phase as possible for the reactants to interact with. However, producing a catalyst made entirely of the active phase would not be economically viable due to the cost of cobalt. This necessitates the inclusion of a support phase of a less costly material. In the Yara catalyst, ceria was chosen as support because of low solubility and low diffusion coefficient of cobalt cations into cerium. X-Ray diffraction analysis has indicated that there are no Ce-Co oxide formations, even at temperatures of 900°C [2]. Furthermore, the ceria oxide was tested without an active phase and, unlike other support candidates that were tested, found to provide a slightly increased conversion rate by itself, which gives additional incentive to employ it as support.

2.5.1 Crystal Structure of Ceria and Co_2AlO_4

CeO_2 is a crystalline oxide material in a fluorite structure, which is cubic with a lattice parameter of $a = 5.411 \text{ \AA}$ [24]. The fluorite structure is displayed in Figure 2.12a. It has a 12 atom unit cell, with the Ce atoms in the face centered positions, and the oxygen occupying the interstitial space inside the cubic cell and forming a cube of sides $a/2$.

The expected reflections to be observed from such a unit cell can be calculated with the structure factor. The relative atomic positions in the unit cell are as follows:

Cerium: $(0,0,0)$, $(1/2,1/2,0)$, $(1/2,0,1/2)$, $(0,1/2,1/2)$

Oxygen: $(1/4,1/4,1/4)$, $(3/4,1/4,1/4)$, $(1/4,3/4,1/4)$, $(1/4,1/4,3/4)$, $(3/4,3/4,1/4)$,
 $(3/4,1/4,3/4)$, $(1/4,3/4,3/4)$, $(3/4,3/4,3/4)$

Assuming kinematic scattering and inserting these into (2.10), with form factors f_{Ce}

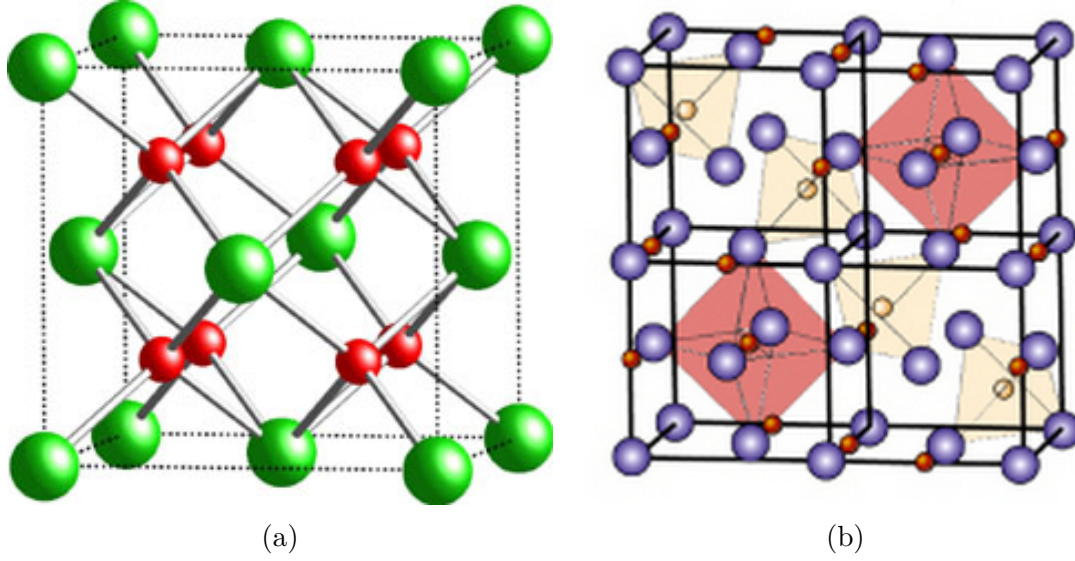


Figure 2.12: (a): The fluorite structure. For cerium dioxide the corner and face atoms are cerium atoms and the inner cube is made up of oxygen atoms. (b): Half a unit cell of the spinel structure, with the octahedral and tetrahedral sites illustrated. For Co_2AlO_4 the sites of blue is O^{2-} , yellow is Co^{2+} and red is either Al^{3+} or Co^{3+} . Images from [25] [26]

and f_O for cerium and oxygen, respectively, this yields

$$F(Q) = \begin{cases} 4(f_{Ce} + 2f_O) & hkl \text{ all even and } h + k + l = 4m \\ 4(f_{Ce} - 2f_O) & hkl \text{ all even and } h + k + l = 4m - 2 \\ 4f_{Ce} & hkl \text{ all odd} \\ 0 & \text{else,} \end{cases}$$

where m is an integer. It follows that CeO_2 will exhibit extinct reflections corresponding to that of a fcc; only allowed reflections are those of hkl all even or all odd.

Co_2AlO_4 is an oxide belonging to the spinel group, having oxidation states of Co^{3+} , Co^{2+} and Al^{3+} . Its cubic structure has a lattice parameter of $a = 8.086 \text{ \AA}$ [27][28]. The spinel structure is based on a fcc cubic structure of oxygen, where the cations occupy $1/2$ of the octahedral holes and $1/8$ of the tetrahedral holes. It has been reported that the inverse spinel structure is energetically favoured for Co_2AlO_4 at $T = 1200 \text{ K}$, with the trivalent Al favoured in octahedral sites and Co occupying both octahedral and tetrahedral sites [29]. The catalytic activity of cobalt in a spinel structure has been found to favour cobalt located in the octahedral sites [30].

The first visible reflections of both materials, as well as some other relevant cobalt phases, are listed in table 2.2. The listed reflections assumes kinematic conditions, which does not necessarily apply to TEM.

Table 2.2: First visible reflections and their respective interplanar spacings (\AA) of CeO_2 , Co_2AlO_4 , CoO , Co_3O_4 , hexagonal metal Co, and cubic metal Co, according to [24], [27] and [31].

CeO_2 $a = 5.411$		Co_2AlO_4 $a = 8.086$		CoO $a = 4.260$		Co_3O_4 $a = 8.084$		Co (hex) $a = 2.507$ $c = 4.070$		Co (cubic) $a = 3.545$	
(hkl)	d	(hkl)	d	(hkl)	d	(hkl)	d	(hkl)	d	(hkl)	d
111	3.12	111	4.67	111	2.46	111	4.67	100	2.16	111	2.05
200	2.71	220	2.86	200	2.13	220	2.86	002	2.02	200	1.77
220	1.91	311	2.44	220	1.51	311	2.43	101	1.91	220	1.25
311	1.63	222	2.33	311	1.28	400	2.02	110	1.25	311	1.06
400	1.35	400	2.02	222	1.23	440	1.43	103	1.15	222	1.02

2.5.2 Synthesis and Implementation

The process of making pellets involves making a slurry containing catalyst and support material, milling to decrease ceria particle size, adding a pore former, spray drying into small spherical granulates, pressing and tableting, and thermal treatment (calcination) at 900°C . In its final form the catalyst is a cylindrically shaped pellet of 9 mm diameter and height, perforated with seven 1.8 mm channels. The channels are made to increase the external surface to the gas. The pellets are seen in Figure 2.13.



Figure 2.13: Pellets of the catalyst. Image from [2].

The pellets are implemented in the process by inserting them into the reactor in a bed a few centimetres thick. Here it also serves as a mechanical supporting structure for the platinum grid, which catalyses the main reaction of ammonia oxidation. The

relatively large size of the pellets increases the voids in between them, thereby also achieving a relatively low pressure drop across the pellet bed. Additionally, the pellets are porous to a certain extent. The pore former used in this process is corn starch, which is removed by the thermal treatment and leaves behind approximately circular pore-canals of a few microns diameter. This leads to a higher mass flow through them, consequently exposing more surface on which the catalyst particles can interact.

The catalyst will typically hold temperatures of 800-900°C in operation. It will in practice also be subjected to extreme temperature changes in short spaces of time due to occasional, inevitable reactor shutdowns.

Chapter 3

Method

3.1 Instrumentation

TEM imaging was carried out on a JEOL JEM-2100 instrument. The microscope was equipped with a LaB₆ filament as the electron source and was not corrected for spherical or chromatic aberrations. Images were captured on a Gatan Orius CCD camera with 2048x2048 pixels. All results were obtained using an acceleration voltage of 200 kV.

STEM images were obtained with a JEOL JEM-2100F instrument. It was equipped with a Schottky field emission gun (FEG) as the electron source, which produces a brighter and generally better probe than the LaB₆ for STEM imaging purposes. Optics were not corrected for aberrations. An acceleration voltage of 200 kV was applied.

Both the JEM-2100 and JEM-2100F was equipped with the Oxford X-Max 80 SDD EDS with a solid angle detection range of 0.23 sr.

SEM was performed on a Hitachi S-5500 microscope. The microscope was installed in a cleanroom environment. It was equipped with a cold-FEG filament for electron illumination. Images were obtained using detectors for secondary electrons, backscattered electrons and BF/DF diffracted electrons. Different acceleration voltages were tested but all results were obtained using 30 kV for best resolution with SE imaging.

3.2 Samples and Sample Preparation

Six samples in total were investigated. The samples were made from two grades of support oxide, a high surface grade and a low surface grade. Catalyst samples

from both support grades were provided in three variants each: support oxide only, unused catalyst, and used catalyst. The supports in themselves were provided in the form they were bought by Yara from the manufacturers, before any treatment and without active material added. Both unused and used catalysts based on the high and low surface ceria supports were provided in their final pellet form. The used catalyst samples had been in stream for 2-3 years.

The two catalyst grades provided correspond to the 'high area grade 1' and 'low area grade 2' of Figure 1.1. Henceforth the samples will be referenced with a HS/LS prefix for samples made from high surface/low surface ceria, respectively, with and added 's' for support material only, 'c' for unused catalysts, and 'u' for used catalysts. The finer high surface oxide was the support used in the commercialised catalyst. An overview of the different sample materials is given in Table 3.1.

Table 3.1: Sample overview and nomenclature.

Sample material	Chemical formula	Notation
High surface catalyst support	CeO_2	HS-s
Low surface catalyst support	CeO_2	LS-s
High surface unused complete catalyst	$\text{Co}_2\text{AlO}_4/\text{CeO}_2$	HS-c
Low surface unused complete catalyst	$\text{Co}_2\text{AlO}_4/\text{CeO}_2$	LS-c
High surface used complete catalyst	$\text{Co}_2\text{AlO}_4/\text{CeO}_2$	HS-u
Low surface used complete catalyst	$\text{Co}_2\text{AlO}_4/\text{CeO}_2$	LS-u

For sample preparation, the catalyst pellets were first ground into fine powders by using mortar and pestle. The two support samples were provided as powders and did not need grinding. All six samples were prepared by solving a small portion of the powder in ethanol or isopropanol. The amount of oxide powder and solvent used was estimated by eye. The solved samples were sonicated in an ultrasonic bath to minimize particle agglomeration.

To make specimens, the particles were dispersed onto grids specifically designed for electron microscopy. The sample material was deposited by carefully dripping the solution onto the grids. Care was taken to solve proper amounts of powder in the solvent, so as to achieve suitably dense particle dispersion on the grids and avoid thick samples of multi-particle thickness.

All TEM/STEM/SEM specimens were prepared using grids of holey carbon film on a 300M copper mesh. The thin carbon film work as a support on which the particles can disperse. The holes in the film allows one to study particles on the edges of them without the carbon in the background. The carbon itself is also useful since it is an amorphous material, which is convenient to use for objective lens astigmatism corrections in the TEM and for adjusting the ronchiogram in STEM.

Chapter 4

Results

The experimental results are presented in the following. The results have been divided into sections after the techniques from which they were obtained, in order of SEM, TEM, and finally STEM.

A TEM overview image of a specimen of the HS-c sample is displayed in Figure 4.1, taken with a small objective aperture. The image is taken in very low magnification and shows almost an entire grid square. The grey perforated sheet is the carbon film. Support and active phase materials are visible as dark particles. The circular white areas are holes in the carbon film, or 'vacuum' since the electron beam does not scatter off any material. The figure shows a typical particle density and dispersion that was obtained on specimen grids.

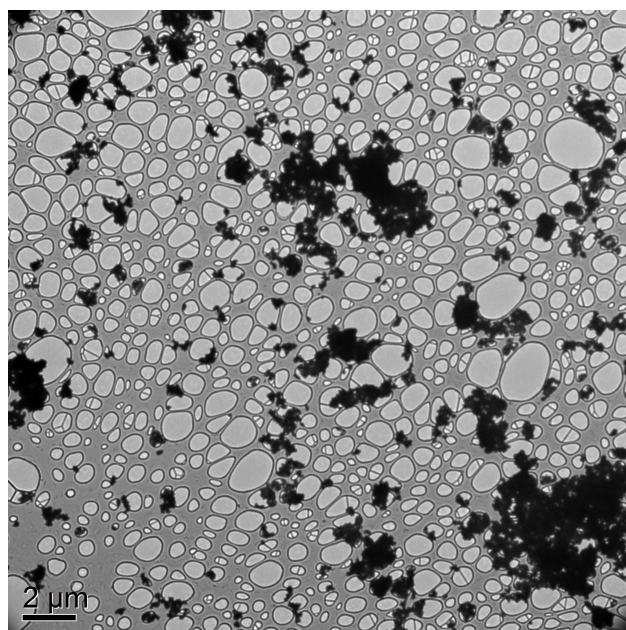


Figure 4.1: TEM overview image of the HS-c sample.

4.1 SEM

The main purpose of the catalyst support material is to provide a surface on which the active catalyst particles can disperse. It could therefore be expected that the effectiveness of the final catalyst to some extent depends on the particle sizes and particle morphologies. It was therefore of interest to investigate these characteristics of the support samples. SEM was used for this purpose because of its ability to image surface characteristics. Because of the low content of active phase of about 2 mole-%, it is safe to assume that the majority of particles seen in any sample at lower magnifications were of the support phase.

Figures 4.2 and 4.3 show SEM images of the samples that were investigated. The images in Figure 4.2 are all taken at x40k magnification except 4.2a', and in Figure 4.3 all images are at x8k magnification except 4.3a'. Note that HS-s sample has been omitted from Figure 4.3 because of the low magnification.

The materials are seen suspended on the holey carbon film of the Cu grids. Particles underneath the film are also seen because the film is translucent for high acceleration voltage of 30 kV.

Figures 4.2a and 4.2b of the HS-s and LS-s support materials, respectively, show a clear difference between the supports. The HS-s sample had much smaller particles compared to the LS-s sample. A higher magnification image of the HS-s support is seen in Figure 4.2a'. The particles have aggregated, either to form agglomerates of particles or sintered structures. Regardless, the surface area is clearly very high for this oxide when compared to the other samples displayed in Figure 4.2. The LS-s support seen in Figure 4.2b was found to be comprised of generally much larger particles. LS-s also had particles of quite diverse morphologies, as seen in Figure 4.3a. Some particles looked like fibrous-like shards, while others could be spherically shaped with what appeared to be mesoporous inner structures, like the particle depicted in Figure 4.3a'.

Of the complete catalyst materials, the HS-c material displayed in Figures 4.2c and 4.3b was found to be made up of the smallest individual particles. In the corresponding used catalyst HS-u in 4.2d, the particle size appeared to have increased slightly.

The LS-c catalyst seen in 4.2e consisted of larger particles than HS-c. LS-c and LS-u samples contained some particles of several micrometer in size, as seen in Figures 4.3d and 4.3e. The difference in particle sizes between LS-c and LS-u is not as significant as in the HS-c/HS-u case.

BE imaging was used to identify the phases in SEM through elemental contrast. Because of its lighter elements, the Co_2AlO_4 phase had lower intensity than the support phase when viewed with BE. This also made it more difficult to identify Co_2AlO_4 particles by BE detection, as any particles of the material was darker than

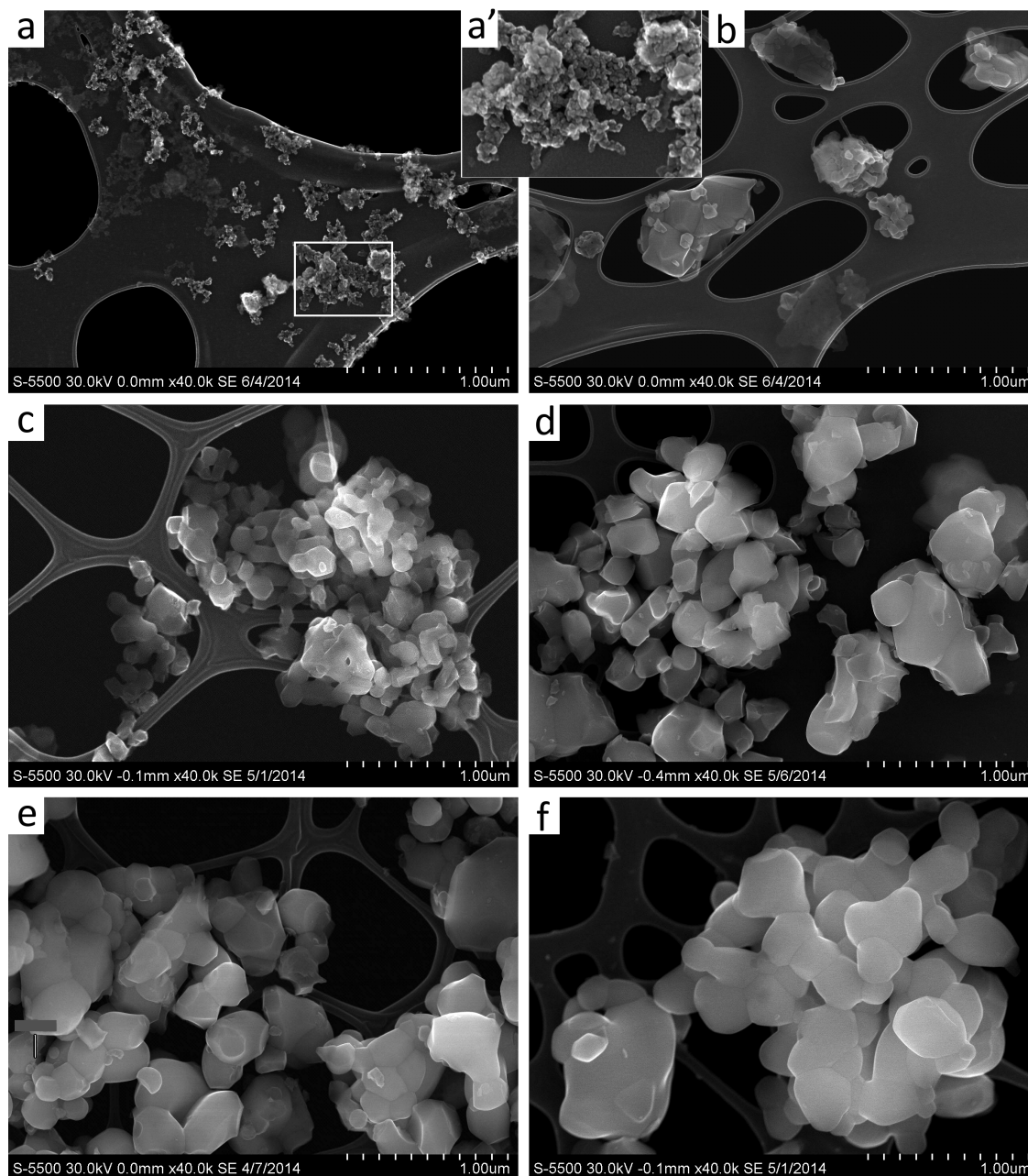


Figure 4.2: SEM images of the catalyst samples at x40k magnification of (a) HS-s, (a') magnified view of the rectangle area in (a), (b) LS-s, (c) HS-c, (d) HS-u, (e) LS-c and (f) LS-u.

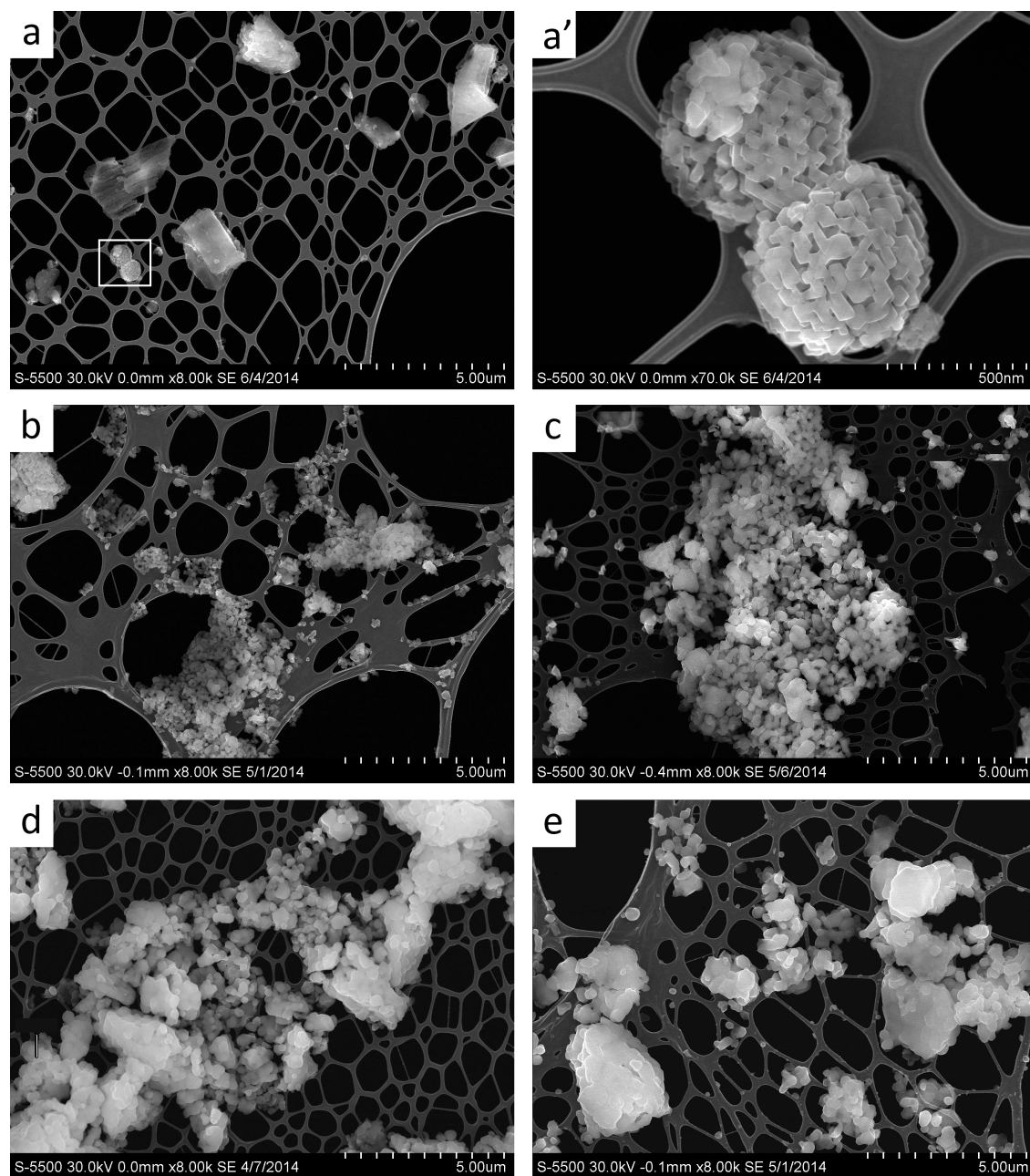


Figure 4.3: SEM images of the catalyst samples at x8k magnification of (a) LS-s, (a') magnified view of the rectangle area in (a), (b) HS-c, (c) HS-u, (d) LS-c and (e) LS-u.

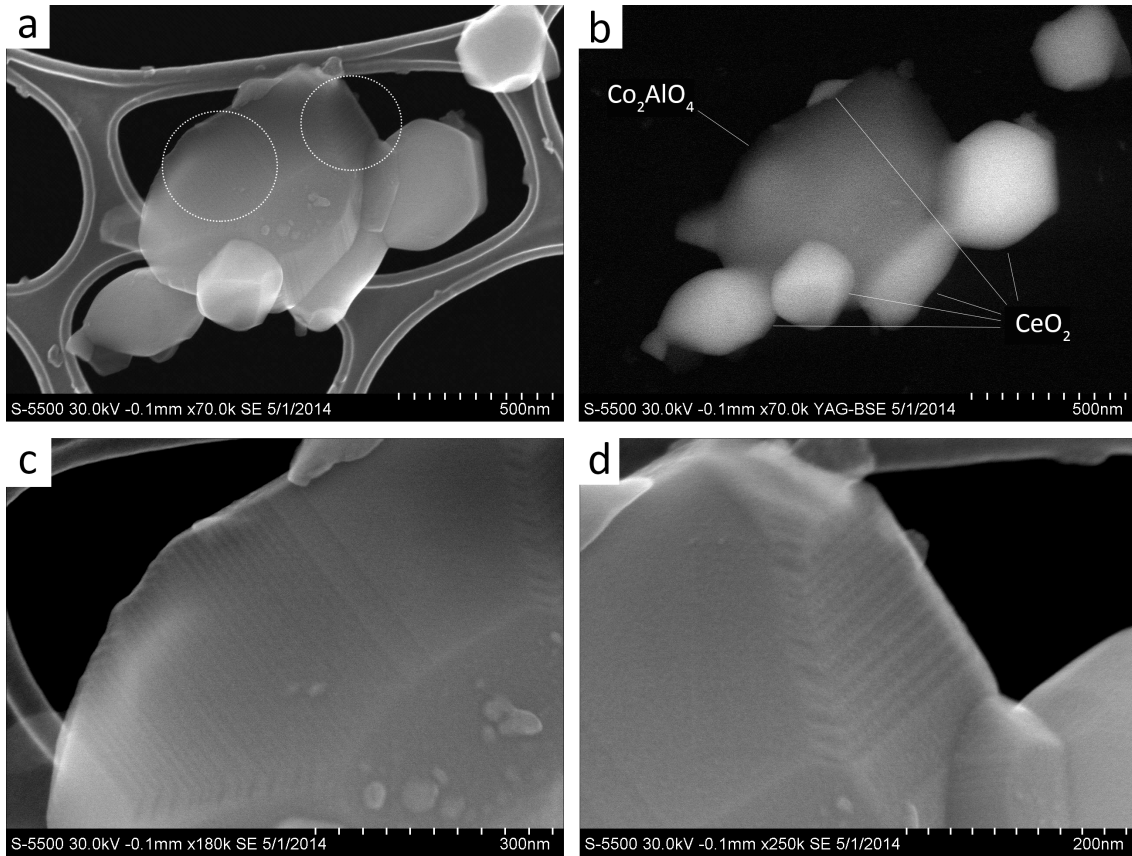


Figure 4.4: Images taken with SEM of (a) LS-u sample with SE and (b) corresponding image with BE, and (c-d) magnified views of the circled regions of (a).

ceria, and against an already dark background (vacuum).

The Co_2AlO_4 phase is depicted in Figure 4.4 from the LS-u sample. The BE image is shown in Figure 4.4b. A clear contrast difference is seen between the large particle and the smaller ones, and the darker appearance of the larger one indicates that it is of the Co_2AlO_4 phase. Despite BEs originating from near the surface of materials, the signal was generally found to be somewhat dependent on particle thickness, being more intense for thicker particles (thickness being inferred from the size seen in the transverse direction of the beam). This was probably because of the relatively high acceleration voltage employed. This corroborates the largest particle being of the Co_2AlO_4 phase.

Incidentally, the Co_2AlO_4 particle of Figure 4.4 is the single largest one observed in any sample, measuring about 880 nm across from the image viewpoint. The particle has some interesting visible surface characteristics visible in 4.4a. Some small particles are seen on the front face. Parts of the surface has straight lines of contrast running in parallel, seen in Figures 4.4c-d.

4.2 TEM

TEM studies were performed on all six samples listed in Table 3.1.

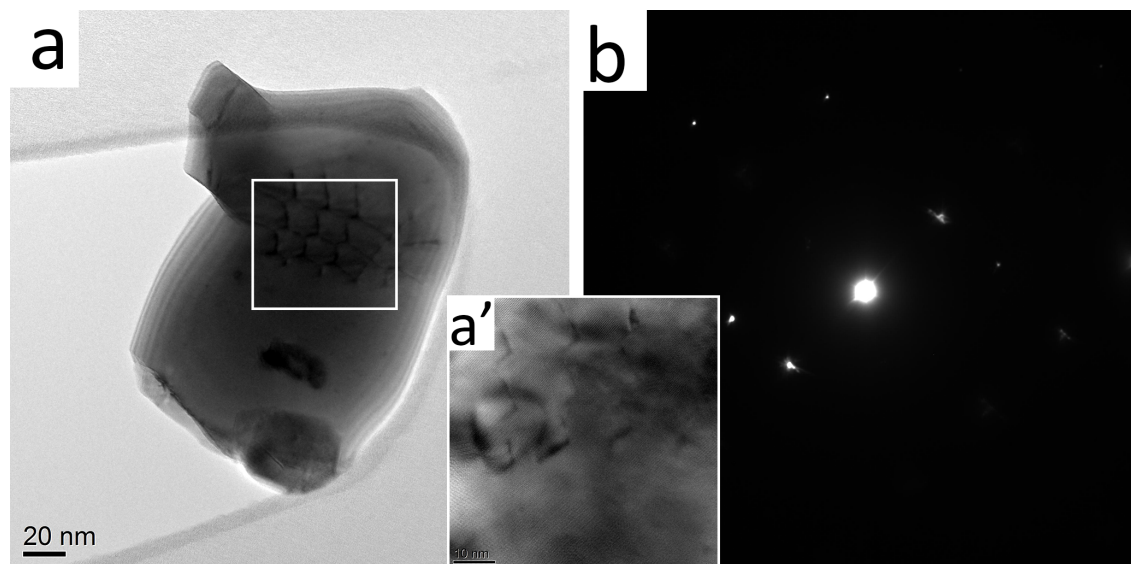


Figure 4.5: The CeO_2 phase from the HS-c sample showing (a) BF image, (a') HRTEM image of the rectangular region in (a), and (b) SAED image of the particle.

Figure 4.5 shows the typical appearance of a particle of the CeO_2 phase in the catalyst samples. In Figure 4.5a a BF image of the particle is seen. The particle appears structurally uniform for the most part, but with some contrast features that stand out. The dark patterns in the middle of the particle are probably dislocations leading to increased scattering. The dislocations are located in between two parts of the particle that appear morphologically different. It could be the result of sintering between two distinct particles leaving crystal imperfections. A magnified view of the patterns is seen in Figure 4.5a'. Here the lattice fringes of the ceria crystal are visible. A SAED image showing the crystal DP is displayed in Figure 4.5b. A few distinct reflections are seen, indicating a very crystalline particle.

The active phase Co_2AlO_4 material appeared as distinct particles in the catalyst samples, typically in a rounded shape. The Co_2AlO_4 particles were always observed clinging to CeO_2 particles in TEM, but the materials appeared to remain separate as particles of distinct shapes.

In TEM low magnification view the support and catalyst materials were not immediately distinguishable, as the particles of the two phases appeared mostly identical. In a higher magnification view, however, the Co_2AlO_4 particles displayed characteristic rough contrast features which made them visually distinguishable from the support phase particles.

Figure 4.6 displays images of the active phase as it appeared in the different samples. From a qualitative consideration, particles observed varied in size ranging from 10 nm to over 800 nm across, most typically in the range 30-200 nm. All particles displayed in Figure 4.6 have some rough contrast features running across them. This is especially prominent in 4.6h, taken from the LS-u sample. Some particles are seen to have rougher surfaces than others, judging from the projected particle edges. Some of these appear to have some surface texture, possibly discrete nanoparticles situated on top of the large particle. These are particularly visible in 4.6f where the optical axis (into the image plane) is parallel to the particle's face. In some of the images the contrast is more dominated by the presence of thick ceria particles that masks the contrast in the Co_2AlO_4 particles.

Some of the particles depicted in Figure 4.6 displayed lattice fringes. These are labelled in the figure. Unidirectional and equally spaced fringes are seen to run across the particles in the parts of them that are contained in the images. In 4.6h, both the (111) and the (220) fringes are visible, indicating that the crystal is oriented with the optical axis along the zone axis $[11\bar{2}]$. Measurement on the fringes in 4.6b gave spacings corresponding to the (200) planes, which are kinematically forbidden reflections. Such fringes are not expected to be seen by themselves, as they are the result of dynamical scattering off of allowed reflections. Measurements on the neighbouring ceria of the image suggest that this could be an erroneous spacing measurement caused by misalignment of the microscope, and not an actual spacing. The fringes in Figures 4.6d and 4.6h correspond to the expected cubic spinel structure of the Co_2AlO_4 material.

Figure 4.7a displays a higher magnification image of the Co_2AlO_4 particle of Figure 4.6c, taken from the HS-u sample. Fine lattice fringes are clearly visible in 4.7a and the zoomed in view of the image in 4.7a'. Two fringes are seen, running orthogonally with respect to each other to create contrast spots. FFT and direct space measurements showed that the fringes corresponds to the (220) and (311) planes, as indicated in Figure 4.7a'.

The DP of Figure 4.7b shows a 2 dimensional pattern of reflections. This indicates a highly ordered monocrystalline particle. DP measurements confirmed that the reflections corresponds to the lattice fringes of the direct space image. The crystal aligned such that it has the zone axis $[3\bar{3}2]$, based on the reflection indexing.

The images of the LS-c material in Figure 4.8 displays two particles of the Co_2AlO_4 phase attached to the ceria support. As seen in 4.8a, these particles are round in shape and about 65 nm and 75 nm in diameter, which is representative to the typically observed size of Co_2AlO_4 particles.

An EDS spectrum of the lower particle is provided in Figure 4.8d. The spectrum shows that particle is dominated by atoms of Co and Al. The ceria peaks are also weakly present in the spectrum due to the nearby support phase. Also seen is a quite strong Cu signal. These signals scatter off the material in the image, but originate

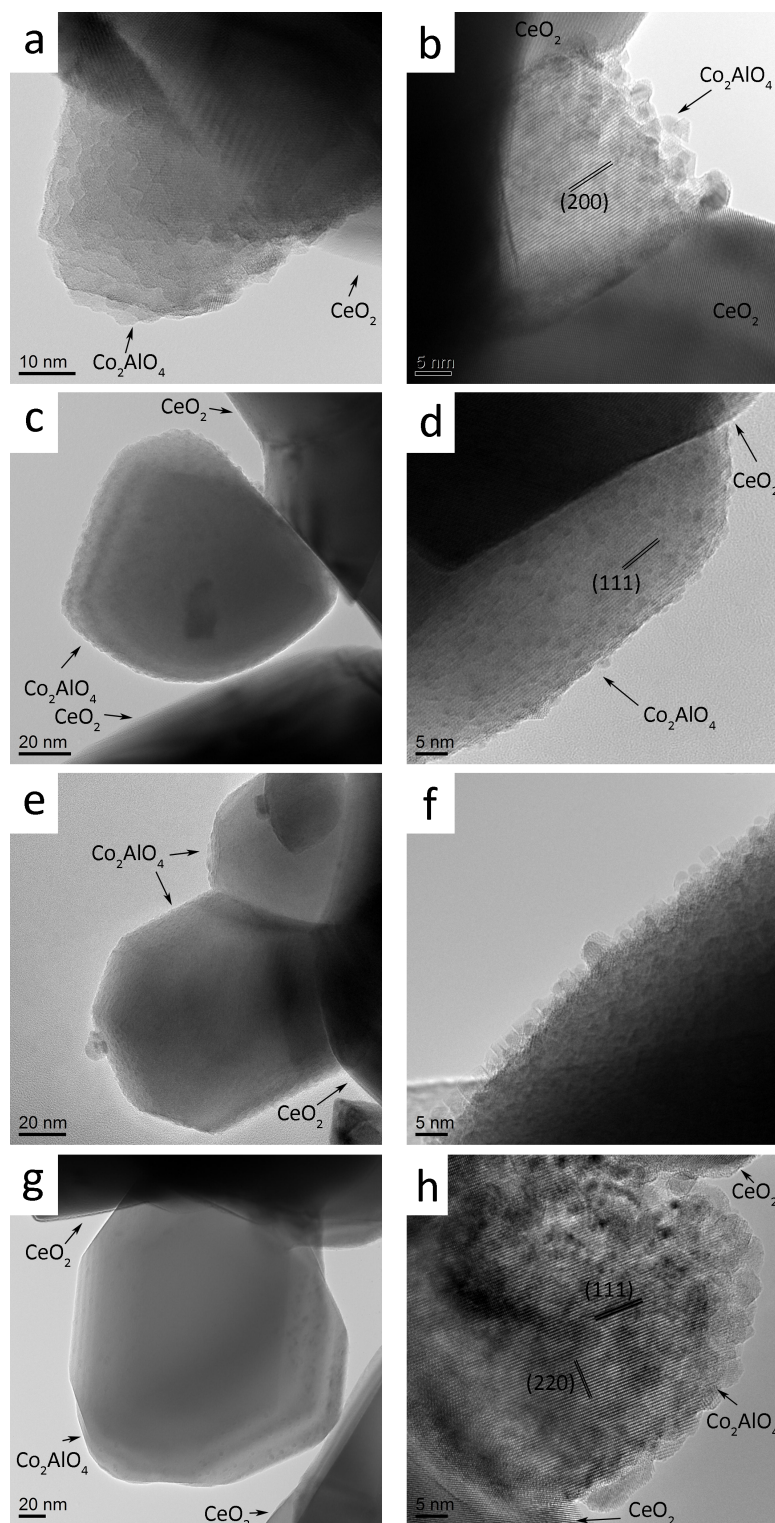


Figure 4.6: The Co_2AlO_4 phase imaged in the different catalyst samples: (a-b) HS-c, (c-d) HS-u, (e-f) LS-c, (g-h) LS-u. Notice the differences in scales.

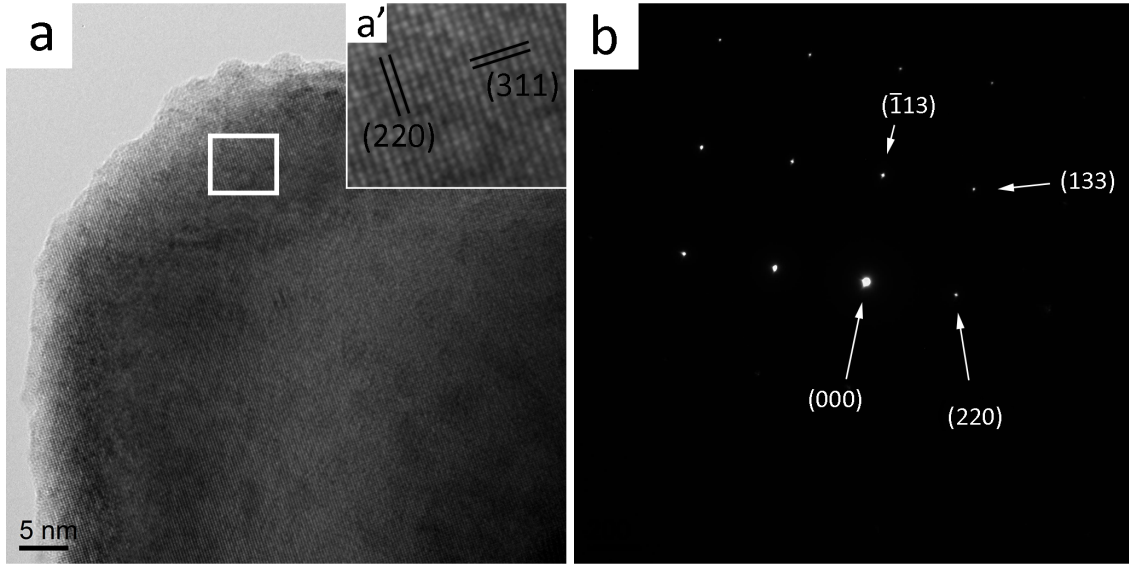


Figure 4.7: Images from the HS-u sample showing (a) HRTEM of a Co_2AlO_4 particle, (a') digitally zoomed view of the rectangle area of (a), and (b) the DP of the whole particle, indexed as a $[3\bar{3}2]$ zone axis.

from the Cu-grid. When working with EDS it was preferred to search near the middle of a grid square in order to reduce the Cu signal as much as possible.

The contact interface between the two phases can be seen in the higher magnification image of the lower particle in 4.8b. The Co_2AlO_4 particle here appears molded and flattened.

Figure 4.8c shows a high magnification view of the same particle. Strong unidirectional fringes are visibly running across the particle indicating crystal ordering. The measurement is presented as # 1 in Table 4.1. The d -spacing shows that the particle is oriented to display fringes of the (111) planes of either Co_2AlO_4 or Co_3O_4 , from Table 2.2. The presence of Al from the EDS spectrum indicates that it is of the expected Co_2AlO_4 phase.

The Co_2AlO_4 particle has a rough appearance to its visible edges, unlike the much smoother edges of ceria particles. The roughness appears to be nanoparticles, <5 nm in diameter, which are separate particles from the large particle. Some of these have visible fringes in the image that were measurable. These are pointed to and numbered in Figure 4.8c, and the measurements of the fringes are presented as # 2-6 in Table 4.1. Particle # 4 stands out as the largest of these (apart from the underlying particle) and its measurement differ from the others. Its fringes come closest to the (111) planes of the Co_2AlO_4 phase, with an error of 3-4%. As seen from Table 2.2, the reflections of Co_2AlO_4 and Co_3O_4 are equal, and which of the phases the particle belongs to can therefore not be discerned from this information. The smaller particles pointed to in Figure 4.8c all have similar spacings, and because

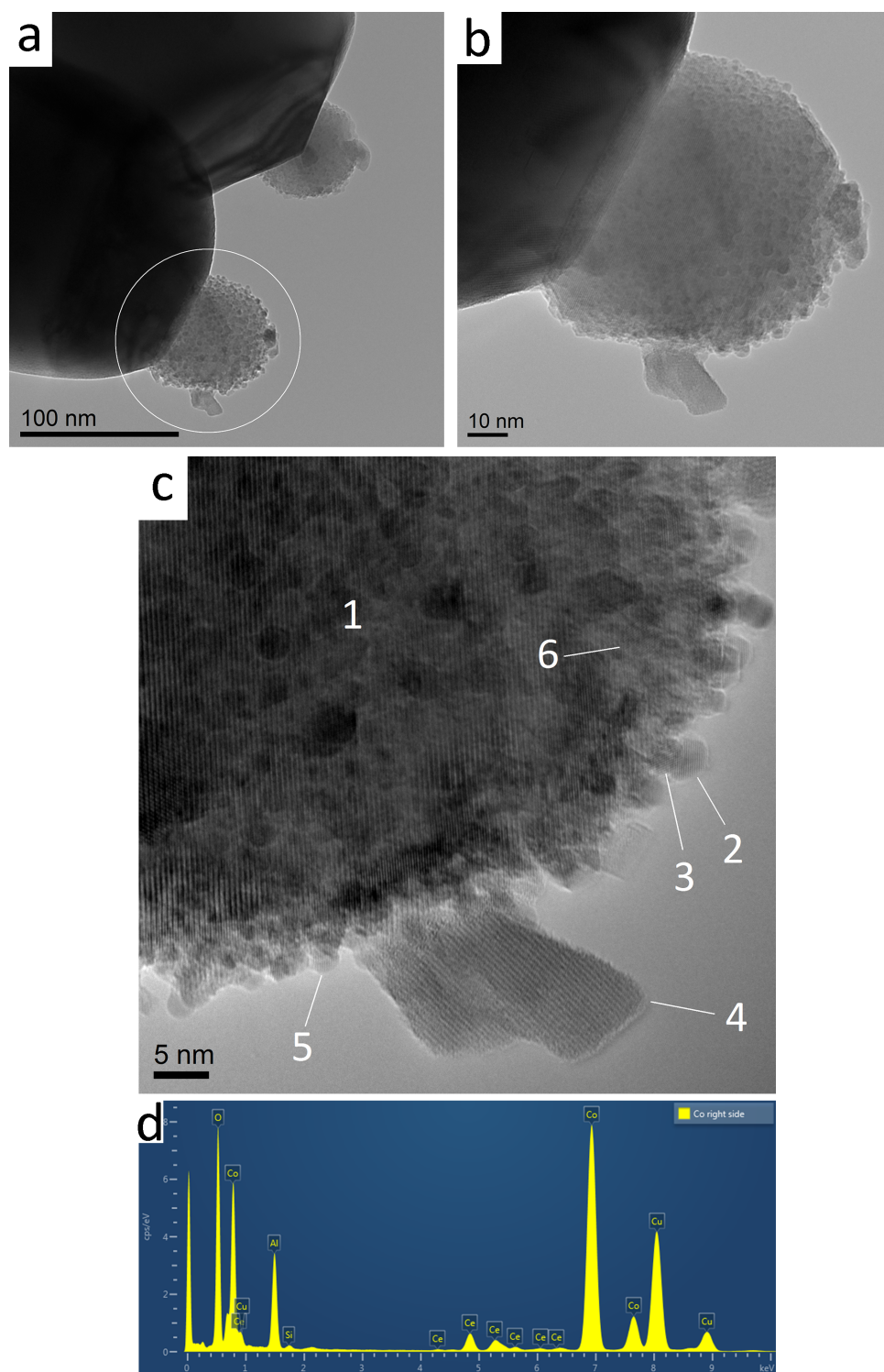


Figure 4.8: TEM view of the LSC sample showing (a) overview image of the Co_2AlO_4 phase attached to the support, (b) magnified view of the highlighted Co_2AlO_4 particle, (c) HRTEM image of the particle with labels indicating areas of visible lattice fringes, and (d) the EDS spectrum of the lower Co_2AlO_4 particle.

they had very few visible fringes which were hard to measure precisely, they could very well be of the same phase. From Table 2.2, the candidate reflections are (400) of Co_2AlO_4 , (400) of Co_3O_4 , (002) of hexagonal metallic Co, or (111) of cubic metallic Co.

Table 4.1: Interplanar spacing measurements from visible fringes on nanoparticles found on the Co_2AlO_4 phase particle on Figure 4.8c. The particle number '# ' refers to the in-figure numeration, and d is the measured spacing (\AA).

#	1	2	3	4	5	6
d	4.69	1.96	2.04	4.51	2.11	2.04

Figure 4.9 displays a site of the LS-u sample with particles from the two phases. A large Co_2AlO_4 particle is observed, 240 nm across at its longest. The dark particle above and the smaller clinging to the Co_2AlO_4 below are of the ceria support. The DP image from a SAED performed on the Co_2AlO_4 particle is displayed in Figure 4.9b. The brightest reflection besides the (000) spot corresponds to the (511) planes of the Co_2AlO_4 structure. Some weaker reflections are seen that originates from the ceria particles, as parts of them were included in the selected area.

The smaller ceria particle is seen in Figure 4.9c. The image illustrates the visual differences that was observed between the materials, with the ceria particle appearing very smooth compared to the Co_2AlO_4 particle that it sits on.

Figure 4.9d inset gives a high magnification view of the particle edge and surface. A quite rough surface is observed, but without any nanoparticles like those which covered the Co_2AlO_4 phase in 4.8. These surface appearances are not unique for either the used or unused samples; different grades of surface roughness and visible nanoparticles were observed in all four samples.

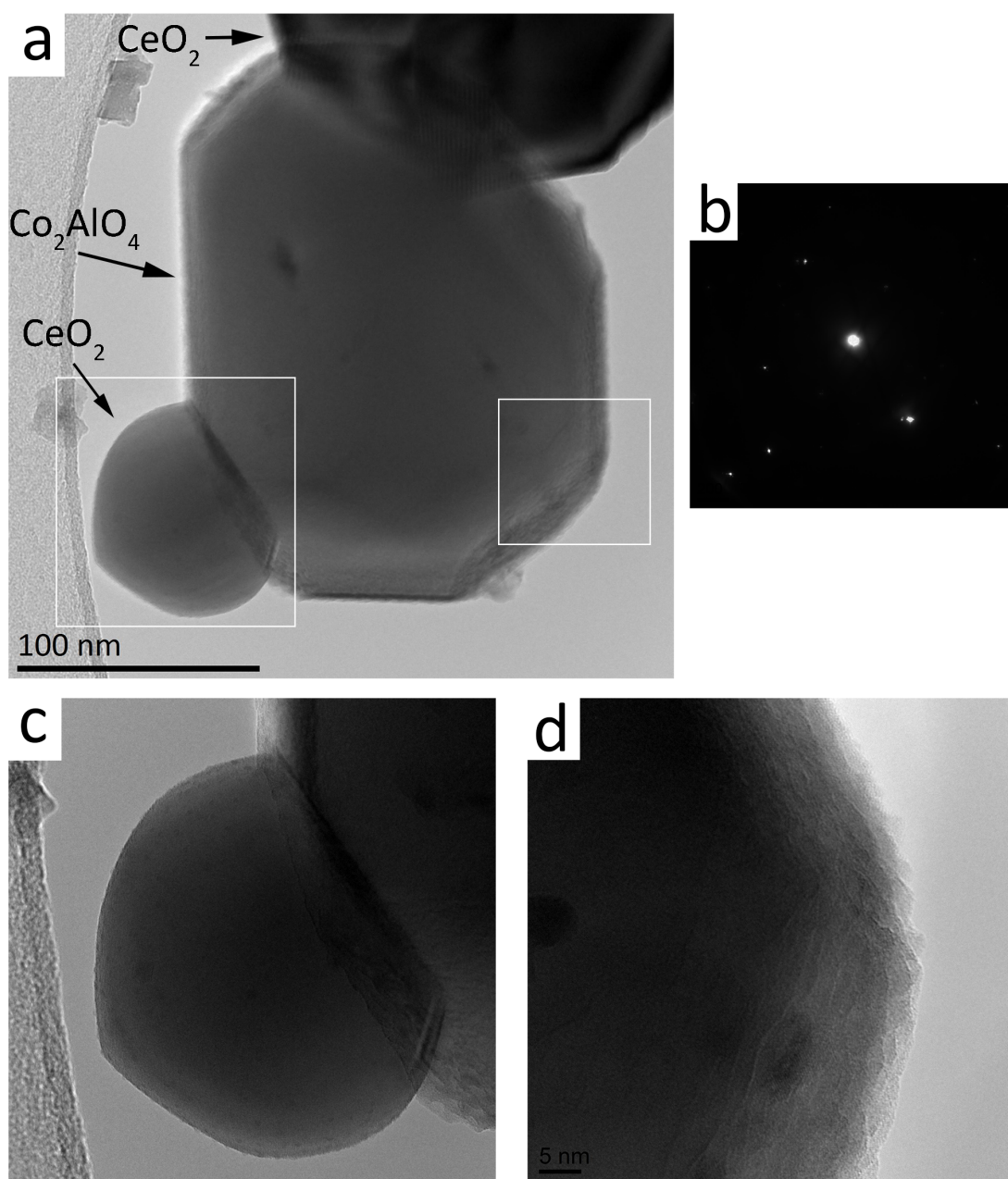


Figure 4.9: TEM images of LS-u, displaying (a) an overview image, (b) SAED image of the middle particle, (c) magnified view of the left rectangle in (a), and (d) magnified view of the right rectangle in (a).

4.3 STEM

STEM combined with EDS mapping was performed to provide analytical imaging of the catalyst system. Two samples were looked at with this technique: HS-c and HS-u. The other samples were not investigated because of time restrictions on the instrument.

Although STEM provides elemental contrast, making it possible to distinguish different phases by their intensity in bright field and dark field, it proved very difficult to identify the Co_2AlO_4 phase from those signals alone. The two phases were too similar in contrast for them to be easily distinguishable. Also, the support phase is heavier than the active phase, so particles of the active phase appeared darker in ADF than particles of the ceria phase, and oppositely in BF. This made the Co_2AlO_4 phase more difficult to spot.

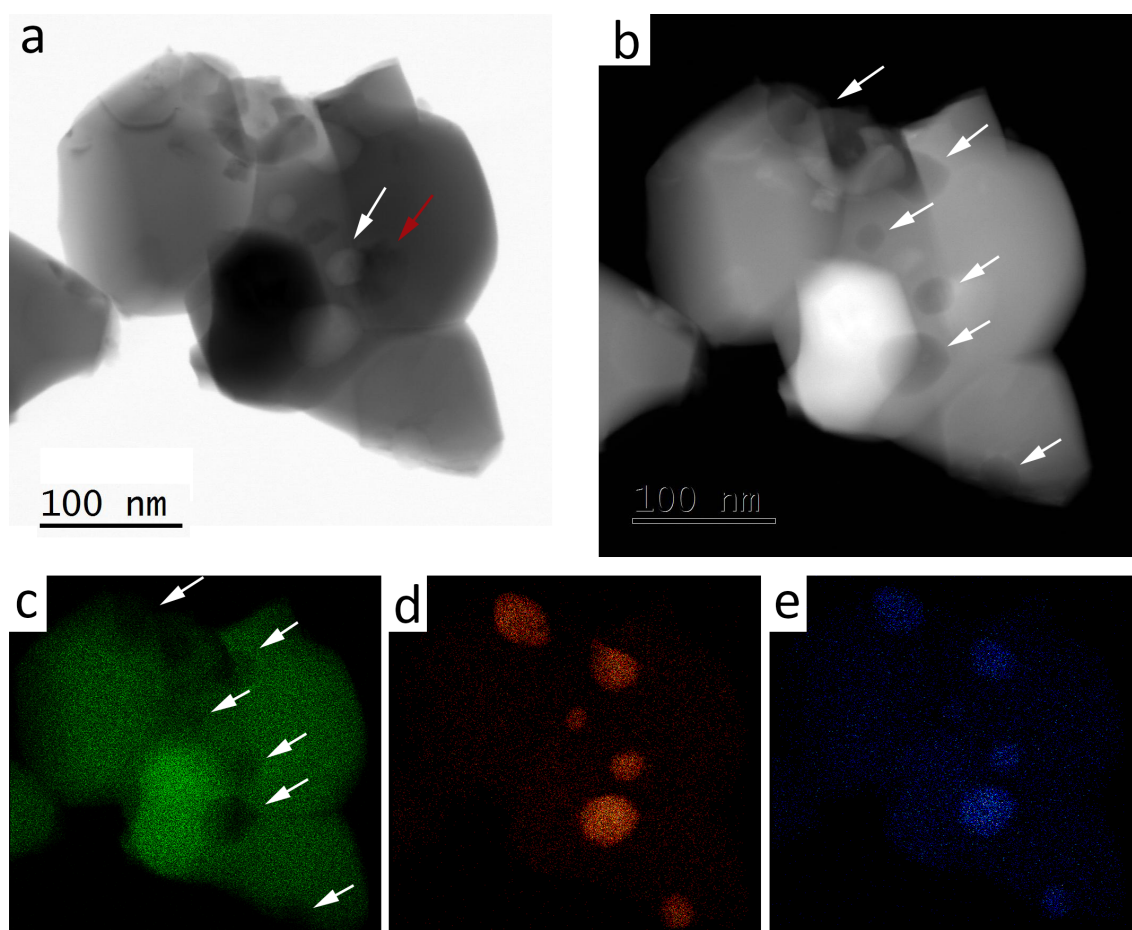


Figure 4.10: Particles of HS-c in STEM showing images of (a) BF, (b) ADF, (c) Ce EDS mapping, (d) Co EDS mapping, and (e) Al EDS mapping.

Figure 4.10 displays images from a STEM/EDS analysis of the HS-c sample. BF

and ADF images of the site is displayed in Figures 4.10a and 4.10b. Figures 4.10c, 4.10d and 4.10e display images of the EDS mapping results of cerium, cobalt and aluminium on the site, respectively. Apparent from the mappings, the Co_2AlO_4 phase in the HS-c material is distributed as somewhat smaller particles on the larger ceria particles. Six particles of the Co_2AlO_4 phase are visible, with dimensions in the range 10-50 nm.

The Co and Al EDS mapping intensities coincide as expected for the Co_2AlO_4 phase. The Al signal is weaker than the Co signal when comparing their mappings, and the particles are not as distinct in the Al map of Figure 4.10e. This is expected because of the lighter atom of Al giving less scattering events, and that there is half the density of Al atoms compared to Co.

Cerium mapping shows that cerium drops in intensity coinciding with the particles, as seen in Figure 4.10c. This indicates that there is less ceria material in the positions where the Co_2AlO_4 particles are found. This could be the Co_2AlO_4 phase sitting in indentations on the ceria surface, or even 'buried' inside. (See Discussion)

The EDS results reveal that the Co_2AlO_4 phase is visible in the DF and BF images of Figures 4.10a and 4.10b, as the presence of Co and Al coincides with areas of slightly different signal intensities. The Co_2AlO_4 phase is found as darker/brighter regions on the ceria particles in the DF/BF images, respectively. This is true for all particles except the larger topmost particle as seen in BF, where the signal darkens. In the BF image of Figure 4.10a, the white arrow points to a particle of Co_2AlO_4 where the contrast is reversed, and the red arrow points to an area of increased intensity of what presumably is ceria on ceria. It is seen that for Co_2AlO_4 on ceria the intensity increases, while for ceria on ceria it decreases.

Figure 4.11 shows images of a site in the HS-u sample that was acquired in STEM. Overview images of the site in BF and ADF is displayed in Figures 4.11a and 4.11b. Mappings of Co and Al seen in Figures 4.11d and 4.11e reveal three particles of the Co_2AlO_4 phase. These are pointed to with white arrows in Figures 4.11b-e. In the Co mapping, a large particle is seen on the lower left side, a smaller one in the upper left side, and one very small, barely visible one near the middle of the image. In Figure 4.11b, a couple of other small spots that resemble particles of the Co_2AlO_4 phase can be seen. A couple of those can arguably be associated with very weak signal congestion in the Co mapping. These are indicated with dark arrows in 4.11b.

The small, topmost, particle is clearly visible in the BF/HAADF images of Figures 4.11a and 4.11b (in the rectangle). It has the most contrast in the HAADF image, which is most sensitive to elemental differences. The high magnification BF image in Figure 4.11f sees the particle lying in the intersection between three dark lines, which are most likely grain boundaries of the ceria crystals. The pattern of contrast running below the particle could be a cascade of dislocations in the ceria, at a grain boundary.

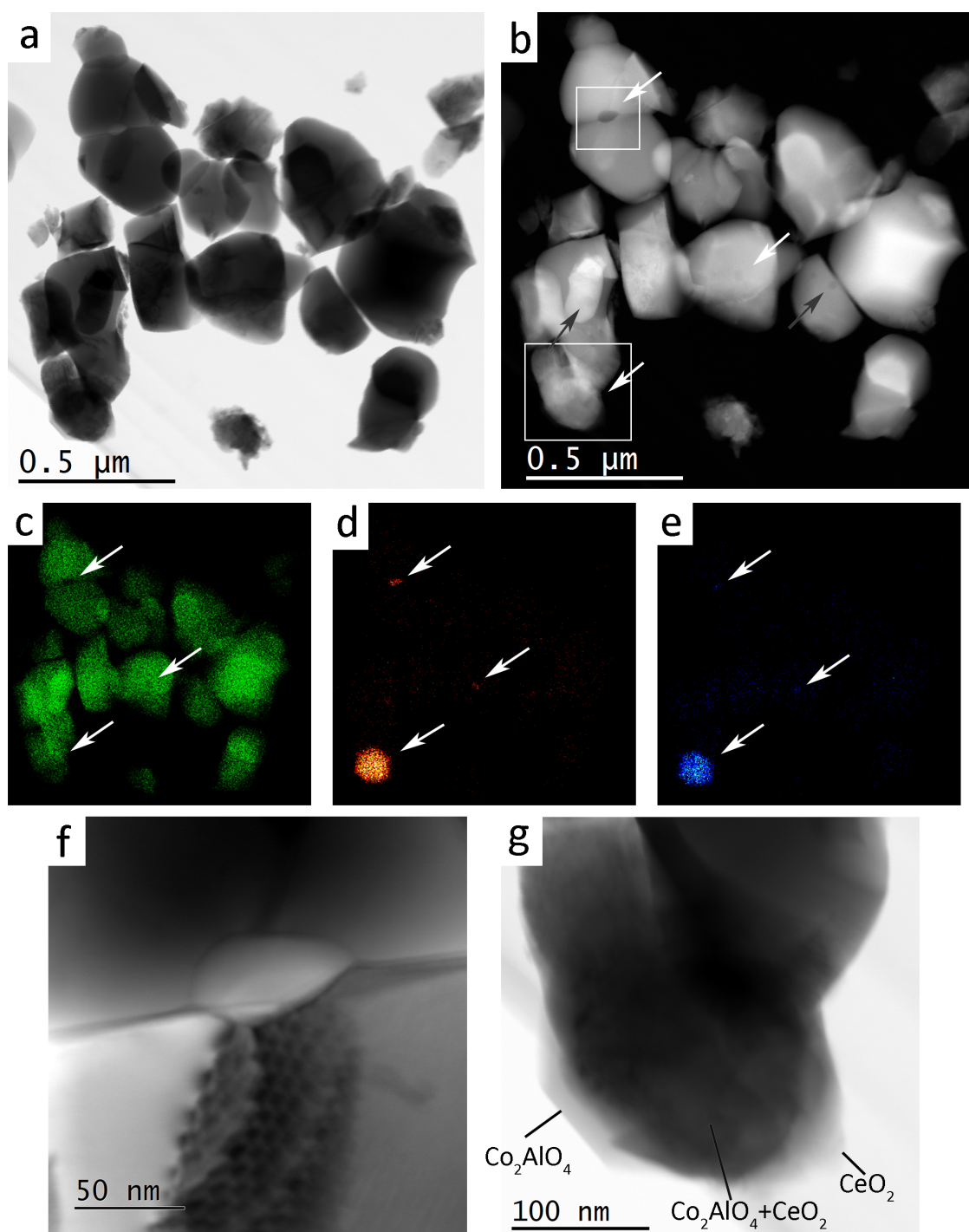


Figure 4.11: Particles of the HS-u sample in STEM showing images of (a) BF, (b) HAADF, (c) Ce EDS mapping, (d) Co EDS mapping (e) Al EDS mapping, (f) BF of the top rectangle in (b), and (g) BF of the lower rectangle in (b).

The lower particle seen in the Co/Al mappings is very difficult to see in the BF/HAADF images, despite being the largest particle with the most intense EDS signals. Even in the higher magnification BF view in Figure 4.11g it is very difficult to discern the shape and outline of the Co_2AlO_4 particle from the support. Closer inspection of the Co mapping shows that the visible edge on the lower left is the Co_2AlO_4 particle, while the visible edge on the lower right side is ceria. The darker region in between is where the particles overlap. This is indicated in the figure ('Co' and 'Ce' indicating the phases Co_2AlO_4 and CeO_2).

Of the three particles indicated with white arrows in Figure 4.11b-e, the two topmost particles behave differently in terms of contrast than the large lower particle. Like what was observed in Figure 4.10, the smaller particles in Figure 4.11 appear as brighter spots where they overlap with ceria in BF. Where the lower particle overlaps with ceria, as seen in 4.11g, it darkens. The Ce signal in Figure 4.11c also appears unaffected by this particle, while it is diminished in the position of the much smaller particle at the top.

The BF and ADF/HAADF images displayed in Figures 4.10 and 4.11 both illustrate the low visibility of the Co_2AlO_4 phase next to ceria in STEM.

Chapter 5

Discussion

In this chapter the results will be discussed and interpreted. The results obtained in the parallel project by Åbø with XRD and BET techniques [32] will be referenced throughout. These are presented in Table A.1 in Appendix A.

5.1 Particle Size and Morphology of the Support Phase

The particle appearances of the samples were demonstrated in Figures 4.2 and 4.3. HS-s was found to be a very fine oxide consisting of very small particles, compared to the LS-s sample which appeared much rougher in the images. The LS-s support also had a wider range of sizes of particles, and with particles of many different morphologies. These curiously shaped particles were not seen in the finished complete catalyst LS-c, and the morphologies are therefore considered unlikely to affect catalytic performance.

There was an observed increase in particle size from the ceria support samples to their respective finished catalysts, especially going from HS-s to HS-c. Change in morphology and size indicates that sintering is prevalent already in the catalyst production during calcination. The significantly larger surface area of the HS-s support is presumably lost to large a degree in the transition to the HS-c catalyst, where the particles have grown significantly. The HS-c catalyst had somewhat smaller particles than the LS-c, and should be expected to lead in surface area.

In the complete catalysts, the ceria particles increased in size from HS-c to HS-u. LS-c and LS-u looked very similar, but also here there could be a slight increase in size. The visible change in particle sizes between fresh and used catalysts suggests that sintering of the support also occurs under reactor conditions. Ultimately, there

is a slight visible difference in roughness in the two grades of used catalysts, HS-u and LS-u.

These results are consistent with the XRD and BET measurements in Table A.1. In particular, from support to catalyst of the HS sample, the average crystallite size had increased by an order of magnitude, while the surface area decreased by a similar factor. The LS samples showed a slight changes in the same properties, but not nearly as significant as for the HS samples.

5.2 Particle Size and Morphology of the Co_2AlO_4 Phase

TEM and STEM results have revealed how the Co_2AlO_4 active phase appears in the system along with the support phase. The support and active material were seen to exist as two distinct phases, with no evidence of diffusion into one another or compound forming between them. The measured interplanar spacings from fringes on the active phase were in agreement with the expected spinel cubic structure of the Co_2AlO_4 material. EDS spectra confirmed the presence of both Co and Al in the particles.

Rough contrast features were clearly visible across the Co_2AlO_4 particles, seen for example in Figure 4.8. It could suggest a porosity to the particles, as have been observed previously in monocrystalline cobalt oxide on coarse alumina supports [31]. However, the particle edges were visibly very rough, which makes it likely that it is a surface roughness and not an inner roughness that causes the contrast.

While all particles of the Co_2AlO_4 phase had rough surfaces, some particles were found to contain small nanoparticles on their surface as well. Some of these nanoparticles contained fringes of different spacings and directionality than the larger particle on which they were situated. Measurements of the fringes were not conclusive, but indicated that these were likely to be of either the Co_2AlO_4 phase or the Co_3O_4 phase. The metallic phases of Co were also possible fits, since the fringes corresponded to their lower reflections, but these are unlikely since they would oxidate. Other techniques will need to be employed to identify the nanoparticle-phase. Since many particles of the active phase were found to contain these nanoparticles on their surfaces, a large part of the total surface area exhibited by the active phase could come from these. The phase of the nanoparticles can therefore be of great importance for the catalytic activity.

Both the general surface roughness and the presence of nanoparticles are expected to increase the effective surface area of the Co_2AlO_4 phase. Increased surface area of particles of the active phase will expectedly increase the activity of the catalyst. Active phase particles containing nanoparticles were found in all catalyst samples,

and it has not been possible to determine if this more common in some samples compared to others.

With the nanoparticles covering some of the Co_2AlO_4 particles' surface, the particles could resemble agglomerates of nanoparticles. However, strong fringes were often seen running across the entire particles, which indicates that each particle was mostly monocrystalline. SADP images such as the one in Figure 4.7b corroborates to this, as they displayed expected patterns and symmetries of the spinel structure.

Co_2AlO_4 particles were found to vary in sizes between about ten nm up to a few hundred nm. The particles of the two phases were of comparable sizes, with ceria particles generally being somewhat bigger than Co_2AlO_4 particles. STEM is often employed for counting and gathering size statistics, but the low elemental contrast between the phases made it difficult to identify particles of the Co_2AlO_4 material. Additionally, the low Co_2AlO_4 content combined with large particle sizes made the amount of particles present in any one frame very few. Thus, it was very difficult to perform quantitative size-distribution analysis of the phase. A possible approach could have been to perform multiple EDS mappings in STEM with low magnification, but it would be a very time consuming undertaking. No attempts were therefore made to measure and count Co_2AlO_4 particles in order to establish size distributions. However, from a qualitative consideration, it is noted that the Co_2AlO_4 particles appeared to be somewhat larger in the used catalysts compared to the fresh catalysts. The Scherrer analysis from the XRD results in Table A.1 were very uncertain for the Co_2AlO_4 material, but the same trend is evident there.

SEM was used for surface characterisation of the Co_2AlO_4 phase. In Figure 4.4, straight lines of contrast are seen running in parallel across a large Co_2AlO_4 particle, with more or less uniform spacings of 10 nm separating them. Given the nature of SE imaging, this must be topological features on the surface of the particle. When the particle surface topology runs in a certain direction relative to the crystal structure, the particle favours to form sharp steps on the surface, instead of a smooth 'slope'. Rather than forming atomic smooth surfaces along an unfavoured crystal direction, the crystal creates steps that are faces of a few tens of atoms long and aligned according to the crystalline arrangement. Small particles are also seen on the front face, ranging from 50 nm down to <10 nm. Even smaller particles could presumably be present but not resolved. The surface roughness and nanoparticles of <5 nm that were seen in TEM were not visible in SEM images. Surface features like these could be important to catalytic behaviour, as it gives larger total surface area, and the exposure of different crystallographic faces can result in different catalytic activities.

Ideally, in a heterogeneous metal supported catalyst, one would want the support particles to be covered in smaller active phase particles, so as to expose as much active surface as possible. If particles of the two phases are of the same size, a large surface of the support will not be much utilised by the active phase for dispersion.

Hence, the surface of the support can not be expected to influence the exposed surface of the active phase to any large extent. The point is nicely illustrated in Figure 4.9, where a particle of ceria is sitting on the much larger Co_2AlO_4 particle, and not the other way around. This is consistent with the reported uncorrelated relationship between support surface area and activity discussed in the introduction chapter (Figure 1.1). However, differences in support roughness are still likely to influence the flow of gases through the pellets, and thus the interaction rate of reactants with the Co_2AlO_4 phase.

The size and rounded shape of the Co_2AlO_4 particles could indicate that a process of sintering is undergone also for this phase. Co_2AlO_4 material could first be present as nanoparticles, like the < 5 nm nanoparticles observed on the surfaces of some of the catalyst particles (see for example Figure 4.6f). During calcination the nanoparticles aggregate and sinter, but leaving some of the nanoparticles on the surface unsintered. A mechanism could be that nanoparticles of a few nm are first produced from precipitation and deposited on the support surface, then agglomerated through surface migration, and finally coalesced into a single crystalline phase. Since mobility for migration typically is high for very small nanoparticles of ~ 5 nm, much of the sintering can occur in the first hours of thermal ageing at high temperatures [33] [34]. This would explain why Co_2AlO_4 particles are so large already in the fresh catalysts, and not just in used catalysts. Because larger particles have smaller surface-to-mass ratios, sintering of Co_2AlO_4 is expected to decrease the activity of the catalyst. Unfortunately, there has not been an opportunity to study the Co_2AlO_4 before it was thermally treated, which would have revealed how the Co_2AlO_4 phase responds to calcination and if it does sinter.

5.3 Embedded Particles of the Co_2AlO_4 Phase

Surprisingly, many of the Co_2AlO_4 particles depicted in projection with ceria were found to decrease the intensity in ADF. This is nicely demonstrated in Figure 4.10b. Particles on the surface of ceria should add to the total material thickness along the optical axis, and would thus be expected to increase scattering, regardless of material. This should give the opposite effect on the intensity in both BF and DF than what is observed for Co_2AlO_4 . However, when small ceria particles were seen on top of a larger ceria particles, the intensity behaved as it was expected to for thicker materials.

The intensity-reversal could possibly be an effect of beam interaction that is not fully understood, for instance an influence of dynamical scattering. However, EDS mappings of Ce in Figures 4.10c and 4.11c showed that there appeared to be less ceria where these particles were situated. A possible explanation is that said particles are not just residing on the surface of the support material, but are partially embedded or completely enclosed in the bulk of it. In this case the Co_2AlO_4 particles do not

add to the thickness, but instead replace matter of ceria in the projection. The dips in Ce signal intensity in EDS is then explained by indentations/cavities in the ceria where the Co_2AlO_4 particles reside. As previously noted, the materials are mutually inert and therefore remain as separate phases, even if one materials particle is embedded into the other material.

If the particles are completely enclosed, it must have occurred during synthesis of the catalyst, specifically during thermal treatment. As noted above, the ceria particles undergo sintering in this step, especially in the HS-s to HS-c case. Smaller particles of ceria could aggregate such that particles of Co_2AlO_4 are caught inside. The ceria then sinters to a single crystal, leaving the cobalt in the bulk of it.

Instead of being completely encapsulated, another possibility is that the Co_2AlO_4 particles are only partially embedded in the ceria. It could be pictured as being 'sunk' into the ceria surface. It would then be protruding from the ceria particle, while indenting its surface. The two phases then act as a single phase in that they 'cooperate' to minimize the surface tension and energy of a heterogeneous particle.

A few Co_2AlO_4 particles were observed to exhibit the opposite contrast behaviour in STEM, indicating that they reside on the surface. The image in Figure 4.11g demonstrates this. The contrast is seen to darken where the Co_2AlO_4 particle and ceria overlap. This particle is clearly not inside the ceria material, based on its size, and also because it is seen protruding on the left side.

Based on what was seen in the limited studies of the HS-c and HS-u materials, particles of Co_2AlO_4 being partially or fully embedded in the ceria could be a common occurrence. All three cases are schematically illustrated in Figure 5.1.

TEM imaging could also have been used to find embedded particles by the use of Fresnel contrast in defocus conditions. This was not realised till after all experimental TEM analysis was completed, however. That no such inner particles are imaged in TEM is not necessarily because they weren't there, but because they were biased against when looking for particles. Co_2AlO_4 particles were looked for specifically at the edges of ceria in order to 1) get the best images of Co_2AlO_4 particles without ceria in the background dominating the contrast, and 2) to confirm the phase of the particles with EDS, where thick ceria particles would have saturated the detector to the point of potentially damaging it.

If encapsulation occurs, as suggested, it can be expected to have large implications for catalytic activity. In case of complete embedding, as illustrated in Figure 5.1c, the initial activity of the catalyst may be lower than otherwise since these particles don't exhibit their surfaces to the reactant gas. On the other hand, these particles could possibly become exposed to the gas at a later stage, when in stream. Particles of the active phase are thus 'preserved', improving longevity. If the particles are instead only partially embedded, as illustrated in Figure 5.1b, only their external

surfaces will contribute to the catalysis. Initial activity of the catalyst will thus be decreased. The embedding could also in this case work to preserve the activity in stream, by 'anchoring' the active particles on the support. Åbø also suggested that the interface between the support and active phase could be a very active site for catalysis [32], based on [35]. In this respect, partially embedded particles will have larger interfaces with ceria, and could therefore increase the catalytic activity.

Because the HS-s and LS-s supports undergoes different degrees of sintering during synthesis, the statistical occurrence and ratio of encapsulated Co_2AlO_4 particles to surface situated particles could be very different for the finished catalysts. There was unfortunately no opportunity to study the LS-c/LS-u catalysts with STEM because of limited time with the microscope.

Further investigations would be needed to confirm that this is indeed encapsulation, as it is hard to make decisive conclusions based on the limited STEM studies performed here. Suggestions are made in Further Work.

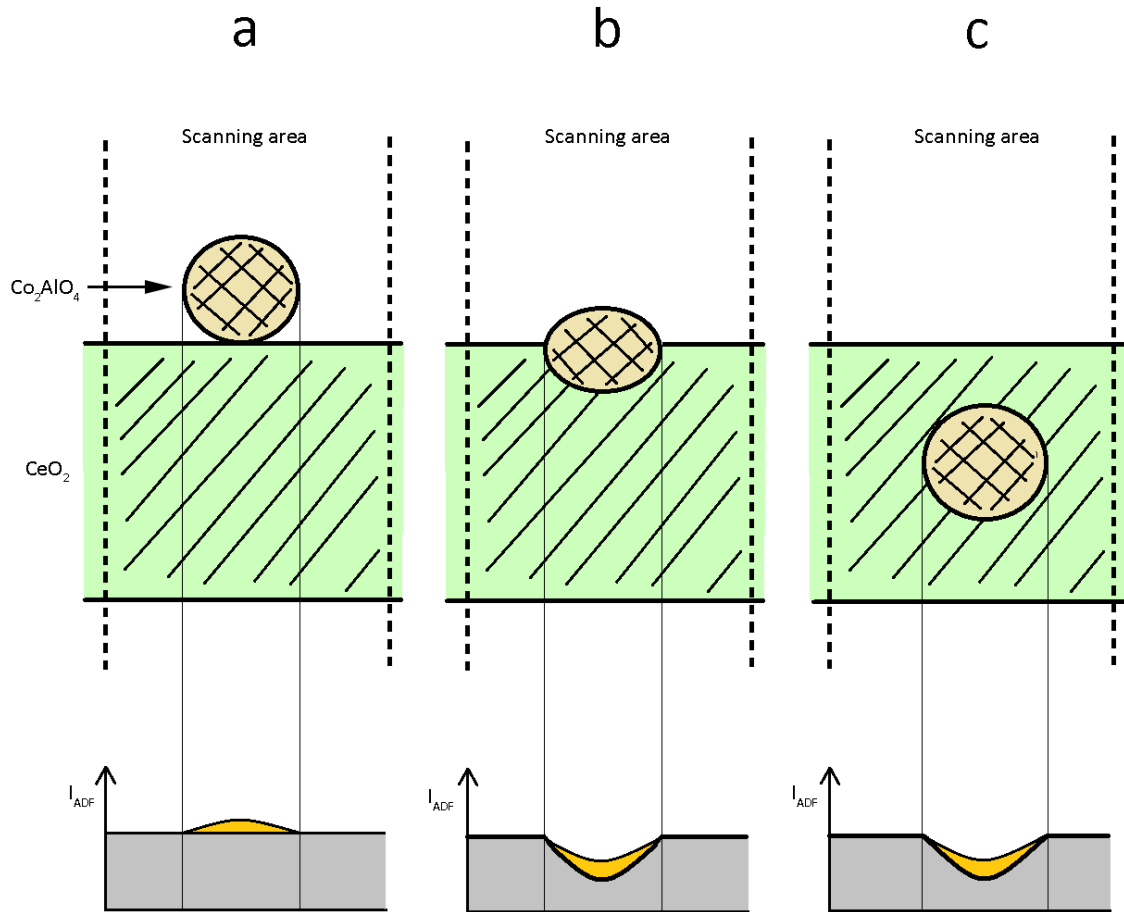


Figure 5.1: Schematic illustrations of the suggested embedding of the Co_2AlO_4 phase in ceria and how it affects the observed intensity in STEM dark field. Cross section views of the materials in a STEM scanning area is shown for three cases, (a) The Co_2AlO_4 particle on top of the ceria, giving increased scattering and detected signal intensity (brightening), (b) the Co_2AlO_4 particle sunk into the surface to be partially embedded, and (c) the Co_2AlO_4 particle encapsulated inside the ceria. (b) and (c) result in a dip in intensity (darkening). In the intensity graphs, the yellow areas indicates the contribution from the Co_2AlO_4 particle.

Chapter 6

Conclusion

In this project an N_2O abatement catalyst, consisting of an active phase Co_2AlO_4 supported on CeO_2 , was studied using electron microscopy techniques. The motivation of the project was to investigate which properties of the cerium dioxide support material that affect the performance of the final catalyst. Six material samples were studied, based on two different supports: the supports by themselves before any synthesis (HS-s, LS-s), the finished catalysts based on said supports (HS-c, LS-c), and the same catalysts that had been used in industrial reactors for 2-3 years (HS-u, LS-u).

SEM images showed that the HS-s support material contained much smaller particles than the LS-s support. This difference had mostly evened out when made into their respective catalysts, where the HS-c and LS-c samples appeared similar in size and morphology. Thus the HS-s support material had undergone the most dramatic change. The HS-c and HS-u materials contained somewhat finer particles than their corresponding LS-c and LS-u samples. Changes in particle sizes are believed to be the result of sintering of the support phase, which occurs both during calcination and in the industrial reactor. SEM SE imaging was used to image the surface of the active phase, showing some fine crystallographic steps in it that could be of interest for catalytic activity.

TEM was applied to image the active phase in the different samples. The active phase Co_2AlO_4 particles were found as distinct particles, with sizes typically in the range 30-200 nm. The two phases did not show any sign of compound forming or diffusion into one another. Particles were found to have rough surfaces, sometimes with nanoparticles of <5 nm diameter attached onto them. It is argued that this could indicate sintering also in the Co_2AlO_4 phase during calcination. The roughness and nanoparticles are believed to increase the activity by increasing the effective surface area. The nanoparticles are believed to be of either the Co_2AlO_4 or the Co_3O_4 structure, but this could not be conclusively determined with TEM. Their phase is believed to be important for the catalytic activity.

STEM combined with EDS mapping suggested that many particles of the active phase could be partially or completely embedded into the bulk of the support phase. The embedding could take place during sintering of the support in calcination, and the difference in support grades could thus influence how the Co_2AlO_4 particles appear in the catalyst. This could have great implications for catalytic activity, both initially and in terms of its durability in reactor conditions.

Chapter 7

Further Work

Some particles of the active phase had distinct nanoparticles on the surface. The composition and phase of these particles are of interest since they could make up large parts of the total exhibited surface area of the active phase. X-ray photoelectron spectroscopy (XPS) can be performed to measure the elemental and chemical composition of the surface. Atomic force microscopy (AFM) could be used for more detailed surface characterisation than what was achieved with SEM here.

The observation reported here regarding Co_2AlO_4 particles being embedded into the bulk of CeO_2 particles will require further investigation through other methods to be verified. The electron tomography technique could be employed, which provides a 3-dimensional view that should be able to verify or reject the suggested embedding. Tomography of the active phase particles should demonstrate if the particle interior is porous or not. STEM/EDS mapping should be carried out on the LS-c/LS-u samples in order to compare them to the results of HS-c/HS-u. Results reported here suggests that the frequency of embedded particles can be lower in the LS-c/LS-u samples, because the rougher support grades have lower degree of sintering.

It has been suggested that the sintering processes during the initial thermal treatment could be important for the catalyst activity. Studying the catalysts in TEM before calcination would allow for comparison of the active phase before and after calcination. In-situ TEM study of the catalyst in calcining conditions could provide valuable information about how the support phase and active phase behave, and possibly how they influence each other, during thermal treatment.

Both STEM and XRD have not been able to provide satisfactory size distributions of the active phase particles. Synchrotron XRD could be employed to obtain crystallographic size information through Scherrer analysis. This could also be set up for in-situ experiments, to see how the phases change under calcination/reactor conditions. Alternatively, the active phase loading could be increased in the samples, but at the risk of changing relevant conditions.

Bibliography

- [1] FAO Production Yearbook. “Food and Agricultural Organization of the United Nations”. In: *FAO Statistics Series* (2013). URL: http://www.fao.org/economic/ess/ess-publications/ess-yearbook/en/#.UrCu6_RDuk4.
- [2] David Waller et al. *N₂O abatement catalyst*. Presentation at Yara International ASA, Porsgrunn 2013. 2008.
- [3] AR Ravishankara, John S Daniel, and Robert W Portmann. “Nitrous oxide (N₂O): the dominant ozone-depleting substance emitted in the 21st century”. In: *science* 326.5949 (2009), pp. 123–125.
- [4] Piers Forster et al. “Changes in atmospheric constituents and in radiative forcing”. In: *Climate change* 20 (2007).
- [5] Freek Kapteijn, José Rodriguez-Mirasol, and Jacob A Moulijn. “Heterogeneous catalytic decomposition of nitrous oxide”. In: *Applied Catalysis B: Environmental* 9.1 (1996), pp. 25–64.
- [6] Øystein NIRISEN et al. *Catalyst for decomposing nitrous oxide and method for performing processes comprising formation of nitrous oxide*. WO Patent 2,002,002,230. 2002.
- [7] Steven S Zumdahl. *Chemical principles*. Houghton Mifflin Company, Boston, 2002.
- [8] *Energy pathway diagram in catalysis example image*. Retrieved December 2013. URL: <http://en.wikipedia.org/wiki/Catalysis>.
- [9] Bård Lindström and Lars J Pettersson. “A brief history of catalysis”. In: *Cat-Tech* 7.4 (2003), pp. 130–138.
- [10] Jens Als-Nielsen and Des McMorrow. *Elements of modern X-ray physics*. John Wiley & Sons, 2011.
- [11] *(hkl)-plane examples image*. Retrieved December 2013. URL: <http://www.helsinki.fi/~serimaa/xray-luento/reciprocal.html>.
- [12] *Braggs law sketch*. Retrieved December 2013. URL: <http://en.wikipedia.org/wiki/File:BraggPlaneDiffraction.svg>.
- [13] David B. Willams and C. Barry Carter. *Transmission Electron Microscopy*. Vol. 1. Springer, New York, 2009.
- [14] Ludwig Reimer and Helmut Kohl. *Transmission electron microscopy: physics of image formation*. Vol. 36. Springer, 2008.

-
- [15] Stephen J Pennycook and Peter David Nellist. *Scanning transmission electron microscopy: imaging and analysis*. Springer, 2011.
- [16] PD Nellist and SJ Pennycook. “Incoherent imaging using dynamically scattered coherent electrons”. In: *Ultramicroscopy* 78.1 (1999), pp. 111–124.
- [17] PD Nellist and SJ Pennycook. “The Principles and Interpretations of Annular Dark-Field Z-Contrast Imaging”. In: *Advances in imaging and electron physics* 113 (2000), pp. 148–204.
- [18] *S(T)EM theory course*. Presentation at NanoLab, NTNU. 2013.
- [19] Hans Schulz. “Short history and present trends of Fischer-Tropsch synthesis”. In: *Applied Catalysis A: General* 186.1-2 (1999), pp. 3–12. URL: <http://www.sciencedirect.com/science/article/pii/S0926860X9900160X>.
- [20] Andrei Y Khodakov, Wei Chu, and Pascal Fongarland. “Advances in the development of novel cobalt Fischer-Tropsch catalysts for synthesis of long-chain hydrocarbons and clean fuels”. In: *Chemical Reviews* 107.5 (2007), pp. 1692–1744.
- [21] Russell S Drago, Krzysztof Jurczyk, and Nicholas Kob. “Catalyzed decomposition of N₂O on metal oxide supports”. In: *Applied Catalysis B: Environmental* 13.1 (1997), pp. 69–79.
- [22] Alessandro Trovarelli. “Catalytic properties of ceria and CeO₂-containing materials”. In: *Catalysis Reviews* 38.4 (1996), pp. 439–520.
- [23] HC Yao and Y Fu Yao. “Ceria in automotive exhaust catalysts: I. Oxygen storage”. In: *Journal of Catalysis* 86.2 (1984), pp. 254–265.
- [24] *Crystallographic and Crystallochemical Database for Minerals and their Structural Analogues*. Institute of Experimental Mineralogy, Russian Academy of Sciences. 2013. URL: [http://database.iem.ac.ru/mincryst/s_carta.php?CERIANITE-\(Ce\)](http://database.iem.ac.ru/mincryst/s_carta.php?CERIANITE-(Ce)).
- [25] *Fluorite structure image*. Retrieved November 2013. URL: <http://www-ssrl.slac.stanford.edu/content/science/highlight/2002-05-31/ssrl-studies-aid-environmental-cleanup-rocky-flats>.
- [26] K Heinz and L Hammer. “Epitaxial cobalt oxide films on Ir (100)-the importance of crystallographic analyses”. In: *Journal of Physics: Condensed Matter* 25.17 (2013), p. 173001.
- [27] JCPDS. *Powder Diffraction File*. 1991.
- [28] P Garcia Casado and I Rasines. “The series of spinels Co₃AsAl_sO₄ (0-s-2): study of Co₂AlO₄J”. In: *Solid State Chem* 52 (1984), 187e90.
- [29] Aron Walsh et al. “Structural, magnetic, and electronic properties of the Co-Fe-Al oxide spinel system: Density-functional theory calculations”. In: *Physical Review B* 76.16 (2007), p. 165119.
- [30] Carlo Angeletti, Franco Pepe, and Piero Porta. “Structure and catalytic activity of Co_xMg_{1-x}Al₂O₄ spinel solid solutions. Part 2. Decomposition of N₂O”. In: *Journal of the Chemical Society, Faraday Transactions 1: Physical Chemistry in Condensed Phases* 74 (1978), pp. 1595–1603.
-

- [31] Roya Dehghan-Niri. “Advanced Transmission Electron Microscopy Studies of Cobalt Fischer-Tropsch Catalysts”. In: (2012). Doctoral Thesis, Department of Physics, NTNU, 2012:216.
- [32] Karl Magnus Åbø. “Investigation of the Yara 58-Y1 nitrous oxide decomposition catalyst”. In: (). 2014. Department of Chemical Engineering, NTNU.
- [33] Abhaya K Datye et al. “Particle size distributions in heterogeneous catalysts: What do they tell us about the sintering mechanism?” In: *Catalysis today* 111.1 (2006), pp. 59–67.
- [34] Thomas W Hansen et al. “Sintering of catalytic nanoparticles: particle migration or ostwald ripening?” In: *Accounts of chemical research* 46.8 (2013), pp. 1720–1730.
- [35] Ewa Iwanek et al. “Direct nitrous oxide decomposition with CoOx-CeO2 catalysts”. In: *Applied Catalysis B: Environmental* 106.3 (2011), pp. 416–422.
- [36] *Dislocation images*. Retrieved December 2013. URL: <http://www2.warwick.ac.uk/fac/sci/physics/current/postgraduate/regs/mpags/ex5/strainedlayer/disloc1/>.

Appendix A

Summary of XRD/BET Results by Åbø

Investigations of this catalyst was performed in parallel between the author and Karl Magnus Åbø at the Department of Chemical Engineering, NTNU [32]. A summary of results obtained by X-ray diffraction and BET adsorption surface area measurements by Åbø is given table A.1. From the XRD spectra the cubic structure parameter was measured and a Scherrer analysis performed to find the mean crystallite sizes of the materials. In the table, the symbol indexes '1'=CeO₂ and '2'=Co₂AlO₄. Note that the τ_2 values are probably somewhat inaccurate because of the low ratio of Co₂AlO₄ in the catalyst (about 2 mole %) and limits to the XRD sensitivity. Comparing $\tau_{2,T}$ to $\tau_{2,EVA}$ for the different samples underlines this point, as they differ dramatically (much more than $\tau_{1,T}$ and $\tau_{1,EVA}$ differ, for comparison).

Table A.1: Results from XRD and BET of the CeO₂ (1) and Co₂AlO₄ (2) phases. a is the measured cubic cell parameter, τ the mean size of the ordered crystalline domains from Scherrer analysis, and BET s.a. is the surface area. Scherrer analysis was performed in two different softwares, Topaz ('T') and EVA, and both results are included.

Sample	a_1 (Å)	a_2 (Å)	$\tau_{1,T}$ (Å)	$\tau_{1,EVA}$ (Å)	$\tau_{2,T}$ (Å)	$\tau_{2,EVA}$ m ² /g	BET s.a.
-	5.412	-	6.5	8.7	-	-	110.2
HS-s	5.412	-	6.5	8.7	-	-	110.2
LS-s	5.412	-	52.0	52.3	-	-	5.5
HS-c	5.412	8.10	67.3	61.1	21.8	21.44	4.6
HS-u	5.411	8.12	79.8	70.2	79.9	58.8	2.3
LS-c	5.412	8.10	92.7	78.6	23.2	74.66	1.4
LS-u	5.411	8.12	95.4	78.6	115.4	69.23	1.3

Appendix B

The Fourier Transform

This chapter is based on the descriptions in Als-Nielsen [10]. The Fourier Transform is an important mathematical tool for material sciences. It appears naturally in the description of scattering processes in matter, while also being the basis of the FFT image processing and filtering algorithm.

The Fourier transform of a function $f(x)$ is mathematically defined in one dimension as

$$\mathcal{F}\{f(x)\} = F(Q) = \int_{-\infty}^{\infty} f(x)e^{ixQ}dx, \quad (\text{B.1})$$

and the inverse Fourier transform is

$$\mathcal{F}^{-1}\{f(Q)\} = f(x) = \frac{1}{2\pi} \int_{-\infty}^{\infty} F(Q)e^{-ixQ}dQ. \quad (\text{B.2})$$

One interesting aspect of the Fourier transform with regards to material physics is the Convolution Theorem. A convolution of two function $f(x)$ and $g(x)$ is defined as

$$f(x) * g(x) = \int_{-\infty}^{\infty} f(x')g(x - x')dx'. \quad (\text{B.3})$$

Roughly speaking, a convolution can be considered a 'smearing' of one function over the other. The convolution theorem reads that the Fourier transform of the convolution of two functions equals the product of their individual Fourier transforms,

$$\mathcal{F}\{f(x) * g(x)\} = \mathcal{F}\{f(x)\}\mathcal{F}\{g(x)\}. \quad (\text{B.4})$$

Conversely, a product of the two functions is equal to the convolution of their transforms,

$$\mathcal{F}\{f(x)g(x)\} = \mathcal{F}\{f(x)\} * \mathcal{F}\{g(x)\}. \quad (\text{B.5})$$

The convolution theorem can be applied to lattices causing scattering to explain features such as line-broadening due to particle sizes and the 'thin foil effect' [10] [13].

Appendix C

Edge and Screw Dislocations

Dislocations are line defects or imperfections of a crystal lattice found at slip planes. An edge dislocation is a sudden termination of a lattice plain, making the surrounding planes having to bend to replace it. A screw dislocation can be visualised as a cut or incision into a crystal where the two sides are displaced by one atomic distance. These dislocations are sketched in Figure C.1.

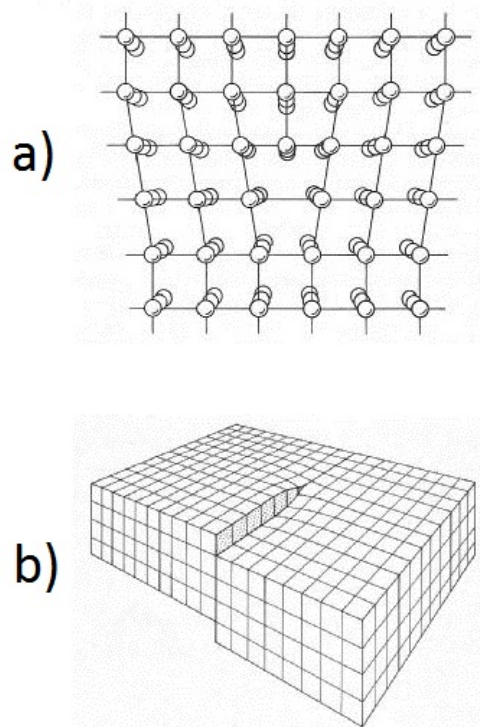


Figure C.1: Sketch of (a) an edge dislocation and (b) a screw dislocation in crystal lattices. Image from [36].